J. Fluid Mech. (2025), *vol.* 1013, A19, doi:10.1017/jfm.2025.10167

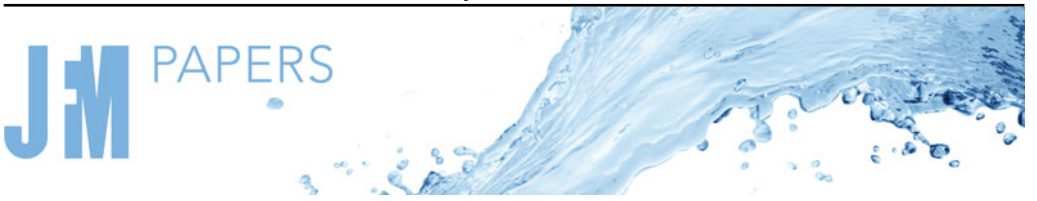

Lateral migration and bouncing of a deformable bubble rising near a vertical wall. Part 2. Highly inertial regimes

Pengyu Shi[1,3], **Jie Zhang**[2] **and Jacques Magnaudet**[1]

[1]Institut de Mécanique des Fluides de Toulouse (IMFT), Université de Toulouse, CNRS, Toulouse, France

[2]State Key Laboratory for Strength and Vibration of Mechanical Structures, School of Aerospace, Xi'an Jiaotong University, Xi'an, PR China

[3]Helmholtz-Zentrum Dresden Rossendorf, Institute of Fluid Dynamics, Dresden 01328, Germany

Corresponding authors: Jacques Magnaudet, magnau@imft.fr; Pengyu Shi, pengyu.shi@toulouse-inp.fr; Jie Zhang, j_zhang@xjtu.edu.cn

(Received 13 January 2025; revised 16 March 2025; accepted 22 April 2025)

The fate of deformable buoyancy-driven bubbles rising near a vertical wall under highly inertial conditions is investigated numerically. In the absence of path instability, simulations reveal that, when the Galilei number, Ga, which represents the buoyancy-to-viscous force ratio, exceeds a critical value, bubbles escape from the near-wall region after one to two bounces, while at smaller Ga they perform periodic bounces without escaping. The escape mechanism is rooted in the vigorous rotational flow that forms around a bubble during its bounce at high enough Ga, resulting in a Magnus-like repulsive force capable of driving it away from the wall. Path instability takes place with bubbles whose Bond number, the buoyancy-to-capillary force ratio, exceeds a critical Ga-dependent value. Such bubbles may or may not escape from the wall region, depending on the competition between the classical repulsive wake–wall interaction mechanism and a specific wall-ward trapping mechanism. The latter results from the reduction of the bubble oblateness caused by the abrupt drop of the rise speed when the bubble–wall gap becomes very thin. Owing to this transient shape variation, bubbles exhibiting zigzagging motions with a large enough amplitude experience larger transverse drag and virtual mass forces when departing from the wall than when returning to it. With moderately oblate bubbles, i.e. in an intermediate Bond number range, this effect is large enough to counteract the repulsive interaction force,

forcing such bubbles to perform a periodic zigzagging-like motion at a constant distance from the wall.

Key words: bubble dynamics, gas/liquid flow, wakes

1. Introduction

In the first part of this investigation (Shi, Zhang & Magnaudet 2024, hereinafter referred to as Part 1), we analysed the results of a series of simulations revealing the mechanisms governing the lateral migration of freely deformable gas bubbles rising near a vertical wall in a liquid at rest. The physical parameters were selected so that bubbles rose at moderate Reynolds number and underwent low-to-moderate deformation, ensuring that they would rise in a straight line in the absence of the wall. However, millimetre-size gas bubbles rising in weakly or moderately viscous liquids, especially water, are subject to path instability (Duineveld 1995; de Vries 2001; Zenit & Magnaudet 2008; Cano-Lozano *et al.* 2016; Bonnefis *et al.* 2023, 2024). Consequently, they usually follow either planar zigzagging or (possibly flattened) spiralling paths, both of which exhibit large-amplitude horizontal excursions. Only small enough bubbles, which do not deviate 'too much' from the spherical shape, can still rise in a straight line when the Reynolds number exceeds a few hundred. These highly inertial regimes, with or without the presence of path instability, are those on which this second part of our investigation focuses.

As discussed in Part 1, interactions between isolated rising bubbles and a vertical wall in moderately inertial regimes are largely governed by two distinct mechanisms. These are the attractive inviscid Bernoulli mechanism, predicted by potential flow theory and resulting from the acceleration of the flow in the gap (van Wijngaarden 1976; Miloh 1977; Kok 1993), and the repulsive vortical mechanism associated with the small flow correction induced by the interaction of the wake with the wall at large distances downstream of the bubble (Takemura *et al.* 2002; Takemura & Magnaudet 2003; Sugioka & Tsukada 2015; Shi *et al.* 2020; Shi 2024). The type of near-wall bubble motion depends largely on the relative magnitudes of the irrotational and vortical interaction mechanisms, which in turn depend on the rise Reynolds number, Re, and the geometrical aspect ratio, χ, of the bubble. Here, Re is based on the bubble's equivalent diameter and rise speed, and χ is the length ratio of the major to minor axes of the bubble. Provided that Re is smaller than a critical value, Re_1, increasing from ≈ 35 at $\chi = 1$ to ≈ 100 at $\chi \approx 1.5$, the repulsive vortical mechanism dominates, causing bubbles to consistently migrate away from the wall. On the other hand, for $Re > Re_1$, both mechanisms remain active, and the bubble is first attracted to the wall down to a certain critical distance at which the total transverse force vanishes, and then undergoes either regular or damped transverse oscillations.

In Part 1, the bubble Reynolds number was kept below approximately 200, and the aspect ratio was, in most cases, smaller than 2. The aim in this second part is to explore the regime in which bubbles rise with Reynolds numbers of $\mathcal{O}(10^2 - 10^3)$, while their aspect ratios may vary from 1 to nearly 3. In such highly inertial regimes, isolated bubbles rising in an unbounded expanse of a weakly viscous liquid are known to undergo a path instability when their aspect ratio exceeds a critical value $\chi_c \approx 2.0$ (Duineveld 1995; de Vries 2001; Veldhuis 2007; Zenit & Magnaudet 2008; Bonnefis *et al.* 2024). Depending on the carrying fluid, the corresponding threshold Reynolds number may vary by more than one order of magnitude, being approximately 670 for water and approximately 110 for a silicone oil five times more viscous than water. Hence, depending on χ, two sub-regimes exist for Reynolds numbers of $\mathcal{O}(10^2 - 10^3)$: a stable one, in which the bubble undergoes

a moderate deformation and maintains a vertical path in the absence of the wall, and an unstable one, in which its oblateness is somewhat larger and leads to an unstable path.

The only investigation to date in the first sub-regime appears to be the experiments by de Vries (2001), some of which were described by de Vries, Biesheuvel & van Wijngaarden (2002). There, bubbles rising near a vertical wall in water were observed to undergo a regular bouncing motion when their equivalent radius, R, exceeded approximately 0.4 mm (corresponding to a Reynolds number in the absence of the wall, Re_∞, of approximately 150). As the bubble size increased further, the amplitude of the transverse oscillations grew. Then, provided R exceeded a second critical value of approximately 0.6 mm (corresponding to $Re_\infty \approx 370$), the bubble, after colliding with the wall, was able to reach a large wall-normal separation and never returned to the wall. Nevertheless, in the initial stages, these 'escaping' bubbles behaved essentially as regular bouncing bubbles, and managed to escape from the wall only after (at least) one period of near-wall bouncing. Clearly, the mechanism promoting the final escape cannot be interpreted as the dominance of the repulsive vortical mechanism summarised above as, if this were the case, the bubble would migrate away from the wall from the very beginning of the interaction sequence. This situation leads to the first objective of this work, which is to clarify the mechanism triggering the escape from the wall of moderately deformed bubbles rising at sufficiently high Re.

On the other hand, bubbles with $\chi > \chi_c$ follow an unstable path even in the absence of the wall. For $\chi \lesssim \chi_c$, results from Part 1 indicate that the vortical mechanism dominates, causing all bubbles with $Re \approx 100$ to consistently migrate away from the wall. Hence, the repulsive vortical mechanism governs the bubble–wall interaction slightly below the onset of path instability. Moreover, the magnitude of the vorticity generated at the bubble surface (hence the intensity of the wake–wall interaction) increases with increasing χ (Magnaudet & Mougin 2007). Given these two arguments, one would expect the dominance of the vortical repulsive mechanism to persist as χ increases beyond χ_c. If so, all bubbles undergoing path instability would exhibit a net migration away from the wall, on which path oscillations would superimpose. This behaviour has indeed been reported in previous numerical simulations (Zhang *et al.* 2020; Yan *et al.* 2022; Mundhra *et al.* 2023) and in the recent experiments by Estepa-Cantero, Martínez-Bazán & Bolaños Jiménez (2024), where bubbles were found to follow either planar zigzagging or flattened spiralling paths while gradually migrating away from the wall. The same behaviour was observed in Part 1 with a bubble with $(\chi, Re) \approx (2.1, 96)$. In these investigations, highly viscous fluids were considered, so that the Reynolds number remained between 100 and 200. In contrast, several experimental studies performed in water (de Vries 2001; Jeong & Park 2015; Lee & Park 2017; Cai *et al.* 2023) considered much larger Reynolds numbers in the range $[700 - 1100]$, corresponding to equivalent bubble radii from 0.97 to 1.96 mm. The observed paths differed dramatically from those described above: instead of gradually migrating towards the bulk, these high-Re bubbles were found to be trapped by the wall, undergoing a zigzagging near-wall motion throughout their ascent. This leads to the second question we wish to examine here, namely the underlying mechanism responsible for the high-Re wall-ward trapping of bubbles. Is it linked to the attractive inviscid Bernoulli mechanism, as in the moderately inertial regimes, or is it specifically related to the interaction between the wall and the double-threaded wake that accompanies zigzagging and spiralling bubbles?

To make progress on the above questions, we carry out a series of high-resolution simulations covering a significant range of hydrodynamic conditions and analyse the different evolution scenarios. In § 2, we formulate the problem, specify the range of parameters we consider and summarise the numerical approach (a series of tests aimed

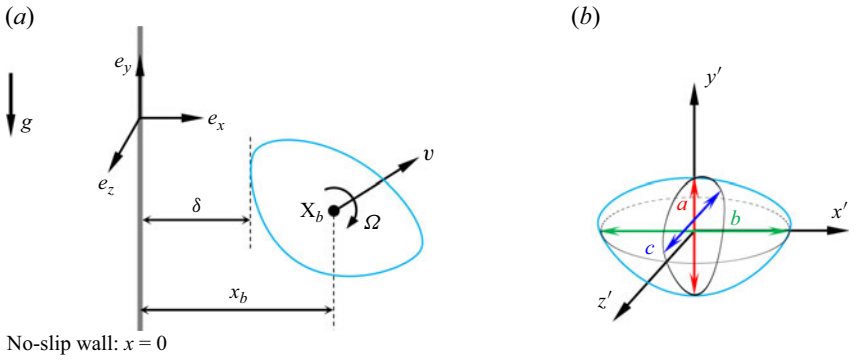

Figure 1. Sketch of the problem. (*a*): flow configuration and basic quantities characterising the bubble motion; (*b*): bubble geometry.

at confirming the adequacy of the grid resolution are detailed in Appendix A). Section 3 provides an overview of the observed scenarios, highlighting the existence of several distinct regimes depending on whether the bubble path is stable or not. The escape scenario observed in the absence of path instability is discussed in § 4, while those found in the unstable path regime, with or without wall-ward trapping, are discussed in § 5. Section 6 summarises the main findings of both parts of this investigation.

2. Statement of the problem and outline of the numerical approach

An initially spherical gas bubble with radius R rises under the effect of buoyancy in a stagnant liquid in the presence of a nearby vertical wall which we assume to be hydrophilic. Figure 1(*a*) specifies the coordinate system, in which the wall lies in the plane $x = 0$. The initial and current positions of the bubble centroid are $\mathbf{x}_{b0} = (x_0, 0, 0)$ and $\mathbf{x}_b(t) = (x_b(t), y_b(t), z_b(t))$, respectively, and the minimum gap between the wall and the bubble surface is $\delta(t)$.

The bubble translational velocity is denoted as $\boldsymbol{v}(t)$, and its possible oscillation frequency is f. Similarly, the local fluid velocity is $\boldsymbol{u}(\mathbf{x}, t)$, the vorticity is $\boldsymbol{\omega}(\mathbf{x}, t) = \nabla \times \boldsymbol{u}$, and the possible spinning rate (to be defined later) of the interface is $\boldsymbol{\Omega}(t)$. Assuming that the gas-to-liquid density and viscosity ratios keep very small values, and that the initial dimensionless separation $X_0 = x_0/R$ is kept fixed (hereinafter $X_0 = 2$, except in some runs examined in § 4 and in Appendix B where the influence of X_0 is investigated), the flow and bubble dynamics may entirely be characterised by the Galilei and Bond numbers, respectively defined as

$$Ga = \rho_l g^{1/2} R^{3/2}/\mu_l, \quad Bo = \rho_l g R^2/\gamma\,, \tag{2.1}$$

where ρ_l and μ_l are the density and dynamic viscosity of the carrying liquid, and γ and g denote surface tension and gravity, respectively. One of the above two control parameters may be replaced with the Morton number $Mo = g\mu_l^4/(\rho_l\gamma^3) = Bo^3/Ga^4$, which entirely characterises the carrying liquid in a given gravitational environment. Once $\boldsymbol{v}(t)$ and f are known, the flow dynamics may be characterised by the instantaneous bubble Reynolds number $Re(t) = 2\rho_l||\boldsymbol{v}(t)||R/\mu_l$ and the Strouhal number (or reduced frequency) $St = 2fR/V_m$, where V_m denotes the time-averaged rise speed. Increasing Bo while keeping Ga fixed primarily increases the bubble aspect ratio, χ. Similarly, increasing Ga with Bo kept fixed primarily increases Re.

In Part 1, we focused on the parameter range $10 \leqslant Ga \leqslant 30$ and $0.01 \leqslant Bo \leqslant 1.0$, which yielded terminal Reynolds numbers $25 \lesssim Re \lesssim 200$ and aspect ratios $1.01 \lesssim \chi \lesssim 2.1$. Here, we consider the more inertial range $30 < Ga \leqslant 90$ and $0.02 \leqslant Bo \leqslant 2$ in which the resulting Reynolds numbers are of $\mathcal{O}(10^2)$ to $\mathcal{O}(10^3)$, and the maximum aspect ratio is up to approximately 2.7. In this parameter range, strongly deformed bubbles with $\chi \gtrsim 2.0$ rising in an unbounded fluid follow zigzagging or (possibly flattened) spiralling paths (Zenit & Magnaudet 2008; Cano-Lozano *et al.* 2016). The corresponding Morton numbers range from 1.2×10^{-13} to 1.0×10^{-5}, i.e. from Galinstan (a liquid metal) to silicone oil DMS-T11 whose kinematic viscosity is ten times that of water at 20 °C.

The results to be discussed below were obtained by solving the three-dimensional time-dependent two-phase Navier–Stokes equations using the open-source flow solver Basilisk (Popinet 2009, 2015). Characteristics of this code and conditions imposed at the various boundaries of the computational domain were discussed in Part 1 and are not duplicated here. Here, we only mention that the flow within the liquid and the bubble is determined by solving the Navier–Stokes equations using the one-fluid formulation, assuming that the interface is free of any contamination. The shape of the interface is governed by the transport equation for the volume fraction of one of the two fluids, an indicator that is also used to compute the local density and viscosity of the two-phase medium according to certain averaging rules detailed in Part 1. Readers are referred to Zhang, Ni & Magnaudet (2021) for details on the governing equations and numerical method, and to Part 1 for specific aspects related to grid refinement, especially in the bubble–wall gap. The computational domain is a cubic box with an edge length $L = 480R$, twice that used in Part 1. This larger size allows us to track the bubble over a sufficiently long vertical distance to examine its behaviour under fully developed conditions. The minimum cell size, Δ_{min}, is decreased down to $\overline{\Delta}_{min} \equiv \Delta_{min}/R \approx 1/68$ close to the interface, and to $\overline{\Delta}_{min} \equiv 1/34$ in the far wake. Following Part 1, the former minimum is further decreased down to $\approx 1/136$ when $\overline{\delta} \equiv \delta/R \leqslant 0.15$ to properly resolve the flow in the gap when the bubble gets very close to the wall. The resolution in the far wake is approximately twice as fine as in Part 1, allowing us to track the details of the wake structure over distances of $\mathcal{O}(10R)$ downstream of the bubble. The adequacy of the grid resolution is confirmed through a grid-independence study detailed in Appendix A. Comparisons between present predictions and experimental results concerning bubbles with non-straight paths rising either in the presence (Estepa-Cantero *et al.* 2024) or in the absence (Duineveld 1995; Tagawa, Takagi & Matsumoto 2014) of a wall are also discussed in this appendix. The good agreement obtained with these experimental results confirms the reliability and accuracy of the numerical approach. However, it must be stressed that even the maximum refinement $\overline{\Delta}_{min} \equiv 1/136$ is not sufficient to properly resolve the flow in the gap when $\overline{\delta}(t)$ becomes extremely small. In such cases, lubrication effects in the gap are not fully captured, leading to what is referred to as a 'bubble–wall collision' in the next sections. It was shown in Part 1 that this under-resolution has virtually no effect on the bouncing frequency and only lowers the maximum separation achieved by the bubble after a 'collision' event by a few per cent.

To roughly characterise the bubble geometry, we need to define the orientation and length a of the minor axis, and the lengths b and c of the major axes in the wall-normal and wall-parallel planes, respectively. To this end, we first consider the wall-normal plane containing the bubble centroid and identify the shortest and longest axes passing through this centroid, following Zhang *et al.* (2021). With this definition, there is in general no reason for these two axes (denoted as x' and y' in figure 1(*b*), respectively) to be strictly orthogonal. The third axis, denoted as z' in the figure, is parallel to the wall and passes also through the bubble centroid. Nevertheless, the maximum horizontal extension of the

bubble in planes parallel to the wall may not lie along this axis if the bubble exhibits asymmetries. To better approach this maximum extension, we identify the length c as that of the longest horizontal segment connecting two points of the bubble surface and lying in the wall-parallel plane passing through the centroid. We are then in position to compute the principal aspect ratio $\chi = b/a$, and the equatorial axes ratio, $\chi_{eq} = b/c$. In order to obtain a global characterisation of the fluid motion at the interface, we also introduce the interface spinning rate, following a suggestion of Rastello *et al.* (2009). Based on the velocity of all fluid elements at the interface, we define this spinning rate, $\boldsymbol{\Omega}$, as

$$\boldsymbol{\Omega}(t) = \frac{3}{2\mathcal{V}_s} \int_{\mathcal{V}_s} \frac{\boldsymbol{r}(t) \times \boldsymbol{u}(\boldsymbol{r}, t)}{||\boldsymbol{r}(t)||^2} \, \mathrm{d}\mathcal{V}_s \,, \tag{2.2}$$

where $\mathcal{V}_s$ is the volume of the thin film made of the computational cells straddling the gas–liquid interface, i.e. those in which the gas and the liquid are both present, and $\boldsymbol{r}(t) = \mathbf{x} - \mathbf{x}_b(t)$ is the position vector with respect to the bubble centroid. Taking advantage of the geometric volume of fluid method employed in Basilisk, the above estimate for the spinning rate may be refined by weighting the integrand in (2.2) by the interfacial area enclosed in each interfacial cell rather than by the cell volume. Tests conducted using this refined definition revealed virtually no difference in the estimated spinning rate in two different regimes, indicating that the definition (2.2) is accurate over the range of parameters considered in this study. The definition (2.2) may be shown to yield the exact spinning rate of a sphere undergoing a rigid-body rotation about one of its diameters. However, bubbles deform over time and the carrying fluid obeys a shear-free condition at their surface, making the angular dynamics of bubbles very different from that of usual rigid bodies surrounded by a fluid obeying a no-slip condition. This is why the term 'spinning rate' must not be misunderstood, as a bubble with $\boldsymbol{\Omega} \neq \mathbf{0}$ may not rotate as a whole. Therefore, in general, $\boldsymbol{\Omega}$ must only be regarded as a three-dimensional measure of the average fluid rotation over the bubble surface.

In the following sections, we make extensive use of dimensionless quantities to describe the flow field and bubble motion. To this end, all variables are normalised using R and $\sqrt{R/g}$ as characteristic length and time scales, respectively. The dimensionless time and local position are denoted as T and $\mathbf{X} = (X, Y, Z)$, respectively, while the dimensionless frequency and position of the bubble centroid are f and $\mathbf{X}_b = (X_b, Y_b, Z_b)$, respectively. Similarly, in the $(\mathbf{e}_x, \mathbf{e}_y, \mathbf{e}_z)$-basis, the ith component of the dimensionless bubble velocity, spinning rate, fluid velocity and vorticity are denoted as V_i, $\overline{\Omega}_i$, U_i and $\overline{\omega}_i$, respectively.

3. Overview of the results

Figure 2(a) summarises in the form of a phase diagram in the (Bo, Ga) plane the various types of near-wall motion observed in the simulations; results for $Ga = 30$ were taken from Part 1. The solid line crossing the phase diagram corresponds to the neutral curve (reproduced from Bonnefis *et al.* 2024), beyond which the bubble path becomes unstable when the fluid domain is unbounded. Figure 3 is the equivalent of figure 2(a) in the (χ, Re)-plane.

3.1. *Below the neutral curve*

We first review the behaviours observed under conditions where the bubble would rise in a straight line in an unbounded fluid, which correspond to cases located below the neutral curve in figure 2(a). Up to $Ga = 50$, the three types of motion already analysed in Part 1 are observed. Specifically, periodic near-wall bouncing takes place at low Bo,

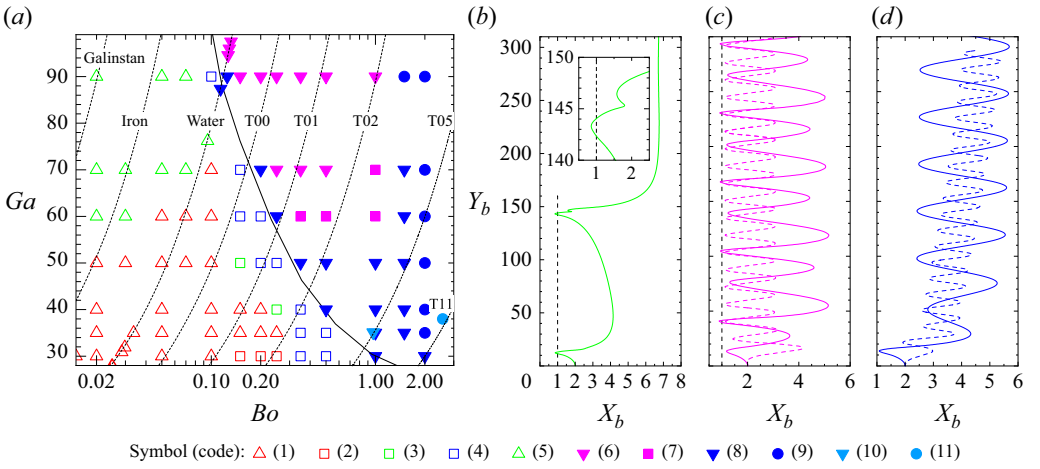

Figure 2. Styles of paths observed in the simulations. (*a*) Phase diagram in the (*Bo*, *Ga*)-plane; (*b*–*d*) typical trajectories illustrating the bouncing–tumbling–escaping (BTE) scenario at (*Bo*, *Ga*) = (0.05, 70), the near-wall zigzagging (NWZ) motion with (solid line, (*Bo*, *Ga*) = (0.25, 90)) and without (dashed line, (*Bo*, *Ga*) = (1, 70)) bubble–wall collisions and the wavy migration away (WMA) scenario with a planar zigzagging path ((*Bo*, *Ga*) = (0.2, 70), solid line; (*Bo*, *Ga*) = (1.5, 50), dashed line), respectively. Solid line in (*a*) is neutral curve corresponding to the onset of path instability in an unbounded fluid (Bonnefis *et al.* 2024); dashed lines: iso-*Mo* lines for different liquids (see table 1 in Part 1 for their physical characteristics). Open symbols, identified with codes (1)–(5), denote cases in which bubbles do not undergo a path instability, with (1) and (2) periodic near-wall bouncing with and without bubble–wall collisions, respectively; (3) damped bouncing; (4) migration away from the wall; (5) BTE. Solid symbols, identified with codes (6)–(9), denote scenarios observed in the presence of path instability, with (6) and (7) NWZ with and without bubble-wall collisions, respectively; (8) and (9) WMA with a planar zigzagging and a (possibly flattened) spiralling path, respectively. Data at $Ga \approx 76$, $Ga \approx 87$ and $Ga \geqslant 94$ in water are taken from experiments by de Vries (2001), while those identified with symbols (10) (silicone oil DMS-T05 at $Ga = 35$), and (11) (water–glycerol mixture at $Ga \approx 38$) are taken from those of Estepa-Cantero *et al.* (2024).

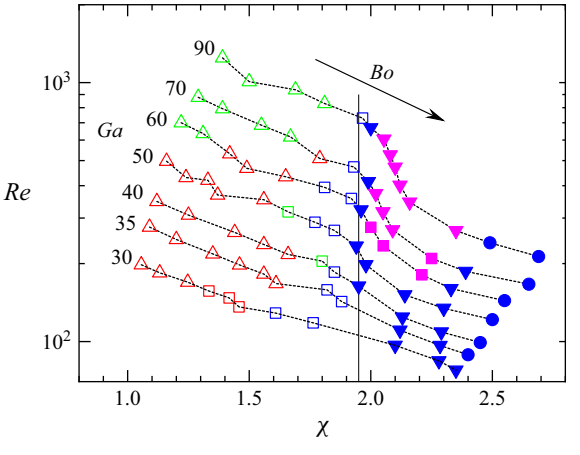

Figure 3. Styles of paths in the (χ, *Re*)-plane. For caption, see figure 2. Vertical line: $\chi = 1.95$; thin dashed lines: iso-*Ga* curves, with *Ga* increasing from 30 to 90 from bottom to top and *Bo* increasing from 0.02 to 2 from left to right on each iso-*Ga* curve. For cases below the neutral curve, values of *Re* and χ are based on final conditions, except in cases with near-wall oscillations, for which average values taken over a single period are used. For cases beyond the neutral curve, values of *Re* and χ correspond to averages taken over one period of the zigzagging or spiralling path in an unbounded fluid.

while a regular migration away from the wall is observed at large Bo, with, occasionally, damped bouncing motions in between. As discussed in Part 1, the mechanisms governing the transition between these three styles of path result from the competition between the irrotational and vortical interaction mechanisms. A new type of motion occurs for $Ga \geqslant 60$, in which the bubble manages to escape the near-wall region after one or two bounces. Figure 2(b) shows a typical path corresponding to this scenario. After two bounces, the bubble briefly migrates towards the wall (as highlighted in the inset of panel b), then quickly departs from it, eventually reaching a wall-normal position $X_b \approx 6.7$ at a vertical position $Y_b \approx 200$. Afterwards, the bubble almost rests at this wall-normal position, its wall-normal velocity exhibiting only minute values. This is because the disturbance induced by a bubble moving at $Re = \mathcal{O}(100)$ decays essentially as the inverse of the cube of the distance to its centroid, following the prediction of potential flow theory. Hence, the presence of the wall is only weakly 'felt' by the bubble in the late stages of its ascent, so that it rises almost vertically as in an unbounded fluid. This path evolution differs from that observed in the damped bouncing regime, where the bubble remains close to the wall throughout its ascent and finally rests at a wall-normal position where the total transverse force vanishes.

This escape scenario specific to highly inertial regimes, particularly the brief wall-ward migration preceding the escape, was observed experimentally in water by de Vries *et al.* (2002) (see figure 5 therein) with an air bubble corresponding to $(Bo, Ga) \approx (0.095, 75.5)$. According to figure 2($a$), this scenario only occurs for nearly spherical bubbles at $Ga = 60$, but quickly dominates the entire region $Bo < 0.1$ when Ga is increased beyond. Figure 3 makes it clear that this scenario is encountered for $Re \gtrsim 600$ and $\chi \lesssim 1.85$. The underlying mechanisms will be discussed in § 4. Here, we just point out that, prior to the escape, a strong vortical layer forms in the vicinity of the bubble surface upon its collision with the wall, causing the z-component of the spinning rate, $\overline{\Omega}_z$, to take large values. This spinning motion yields a sizeable Magnus-like force pointing away from the wall, which promotes the bubble escape. In what follows, we refer to this type of path evolution as the bouncing–tumbling–escaping (BTE) scenario.

To illustrate the influence of the Reynolds number on the style of path, we select a series of results obtained at two specific values of the bubble aspect ratio, $\chi = 1.4$ and $\chi = 1.8$. Figure 4 shows the variations of the wall-normal velocity, $V_x(T)$, with the lateral position, $X_b(T)$, as Re increases by one order of magnitude, from values of $\mathcal{O}(10^2)$ to $\mathcal{O}(10^3)$. For $\chi \approx 1.8$, the bubble migrates away from the wall at $Re = 158$, experiences damped near-wall oscillations at $Re = 204$ and bounces periodically on the wall at $Re = 509$. In these two bouncing cases, the maximum lateral separation between the bubble and wall increases from 3 to 4 as Re increases. At $Re = 792$, the bubble manages to reach a lateral position $X_c = 6.3$, where it rests. The brief wall-ward migration taking place before the escape corresponds to the short period of time when $V_x(T) < 0$ in the loop formed by the corresponding curve. For $\chi = 1.4$, the bubble already experiences periodic near-wall bounces at $Ga = 35$, corresponding to $Re = 218$. At $Re = 531$, while it still undergoes regular bouncing, its lateral motion weakly reverses during the departing stage. The maximum lateral position is $X_b = 5.3$, and this large separation results in a very slow bouncing frequency, $St = 0.0055$. As Re increases further, the bubble escapes from the wall, resting eventually at a lateral position $X_c = 7.3$ at $Re = 793$ and $X_c = 8.8$ at $Re = 1247$.

Figure 4 also allows the effects of the aspect ratio to be appreciated. First, it is seen that, in the two cases with Re close to 200, the less deformed bubble experiences periodic bounces, while that with $\chi = 1.80$ follows a damped bouncing evolution. In the two cases with Re close to 500, both bubbles undergo regular bouncing but their maximum

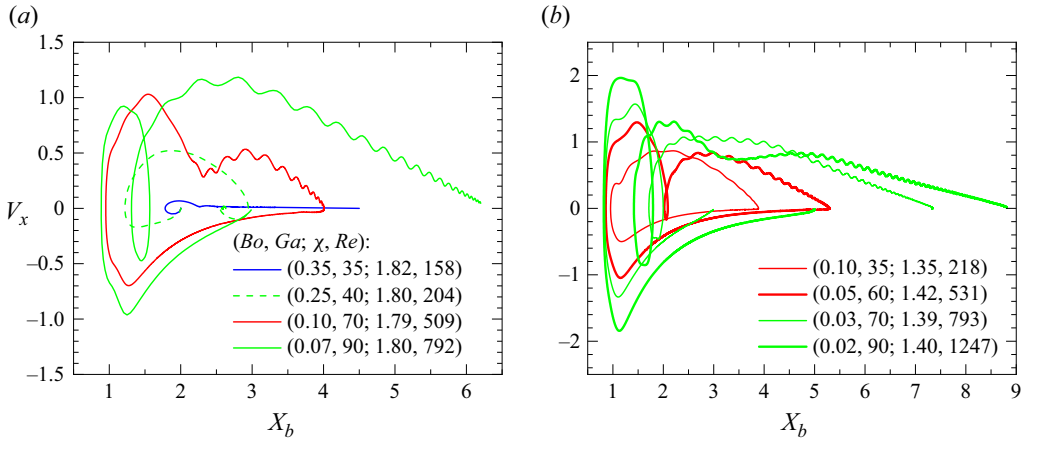

Figure 4. Variations of the bubble wall-normal velocity, V_x, as a function of the bubble–wall distance, X_b, for selected cases at (*a*) $\chi \approx 1.8$, and (*b*) $\chi \approx 1.4$. The corresponding values of Bo, Ga and the resulting Re are indicated in each panel. The initial position is set as $(X_0, V_x) = (2, 0)$. In periodic bouncing cases (red lines), only the variation during the fully developed stage is shown. In BTE cases (solid green lines), only variations during the last cycle of motion, starting at a time when the bubble begins to migrate towards the wall, are shown.

lateral position reduces from 5.3 at $\chi = 1.42$ to 4.0 at $\chi = 1.79$. Accordingly, the reduced frequency increases from 0.0055 at $\chi = 1.42$ to 0.013 at $\chi = 1.79$. Last, when $Re \approx 790$, both bubbles manage to escape from the near-wall region and their final wall-normal position also decreases as χ increases.

3.2. *Beyond the neutral curve*

In figure 3, bubbles with an aspect ratio larger than ≈ 1.95 are found to follow zigzagging or spiralling paths, consistent with the experimental observations of Zenit & Magnaudet (2008). Similarly, in figure 2(*a*), path instability is seen to take place for all (Bo, Ga) sets located beyond the neutral curve determined for bubbles rising in an unbounded fluid. This observation suggests that the presence of the wall plays no role in the occurrence of path instability. However, in its early stage, it selects the orientation of the plane in which the bubble oscillates, making path instability arise through an imperfect bifurcation. Up to $Ga = 50$, all bubbles experiencing path instability migrate away from the wall. We refer to this type of motion as the wavy migration away (WMA) scenario. In this regime, bubbles maintain a zigzagging path in the wall-normal plane up to $Bo \approx 1.5$ (see the examples in figure 2*d*). Then, this path transitions to a spiralling motion at larger Bond numbers. Bubbles following the WMA scenario were observed experimentally by Estepa-Cantero *et al.* (2024). The corresponding data, shown in figure 2(*a*), corroborate the present findings. For $Ga > 50$, the same scenario is encountered both for $Bo > 1$ and within a narrow band of significantly lower Bond numbers lying just above the neutral curve, e.g. $Bo \approx 0.2$ for $Ga = 70$ and $Bo \approx 0.12$ for $Ga = 90$.

When Ga is larger than 50 and Bo is above the aforementioned band but below unity, a new type of motion emerges. In this intermediate range, the bubble is trapped near the wall, ultimately undergoing a near-wall zigzagging-like (NWZ) motion. Bubble–wall collisions due to an incomplete resolution of lubrication effects in the immediate vicinity of the wall (see § 2) occur for $Ga \gtrsim 70$. Two bubble paths typical of this regime, with and without bubble–wall collisions, are shown in figure 2(*c*). Although the upper limit of present simulations is $Ga = 90$, available data indicate that this scenario still holds at

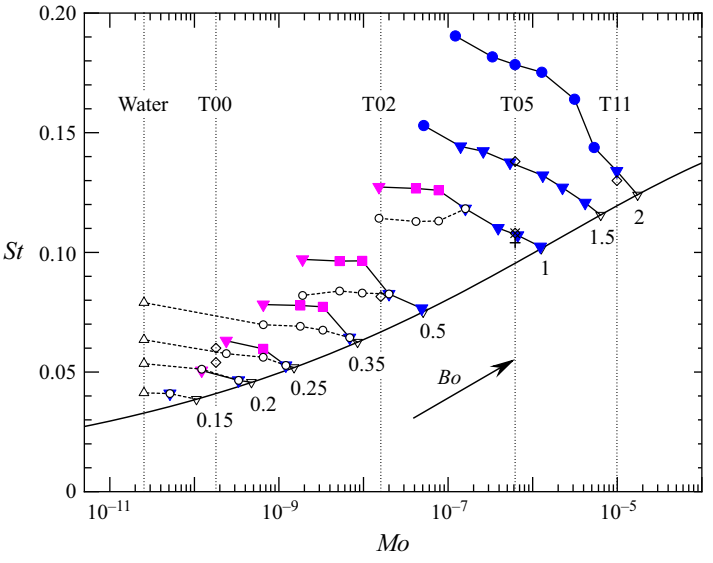

Figure 5. Variation of the Strouhal number, St, of path oscillations as a function of the Morton number. Solid symbols: present results in the wall-bounded configuration (for caption, see figure 2); open circles: present results in an unbounded fluid. Thin solid and dashed lines connect St values corresponding to a fixed Bo and different Ga (hence, Mo) in the wall-bounded and unbounded configurations, respectively. Thick solid line: neutral curve of path instability in an unbounded fluid (Bonnefis *et al.* 2024); ▽: selected values of the critical Strouhal number, St_c, from the same reference; △: experimental data in water (Duineveld 1994, 1995; Veldhuis 2007; Veldhuis, Biesheuvel & van Wijngaarden 2008; Jeong & Park 2015) (values were interpolated from neighbouring Bo). Symbols + and ×indicate data at $Bo \approx 1$ from experiments in silicone oil DMS-T05 by Zenit & Magnaudet (2009) and Estepa-Cantero *et al.* (2024), respectively; ⋄indicates numerical data for various liquids in an unbounded fluid (Cano-Lozano *et al.* 2016).

larger Ga. In particular, it was identified in experiments performed in pure water (de Vries 2001; Jeong & Park 2015; Lee & Park 2017; Cai *et al.* 2023) with millimetre-sized air bubbles corresponding to $95 \lesssim Ga \lesssim 270$ and $0.125 \lesssim Bo \lesssim 0.5$. It is important to stress that the NWZ regime and the near-wall bouncing regime observed for low enough Bo and Ga below the neutral curve (open red symbols in figure 2*a*) are totally distinct. Indeed, although bubbles follow periodic near-wall paths in both cases, the mechanisms governing these two regimes are fundamentally different. In the moderate-Ga near-wall bouncing regime, periodic bouncing is linked to the shedding of a pair of streamwise vortices in the bubble wake, with vortex formation governed by the near-wall shear resulting from the no-slip condition at the wall (see § 4 of Part 1 for details). In contrast, in the high-Ga NWZ regime, lateral oscillations arise due to path instability that would occur even in an unbounded fluid. Furthermore, the mechanism preventing NWZ bubbles from escaping the wall is linked to intense wake–wall interactions, as will become clear in §§ 5.2–5.3, whereas in the moderate-Ga near-wall bouncing regime, bubble entrapment results from the attractive inviscid Bernoulli effect.

Figure 5 shows how the Strouhal number (or reduced frequency), St, of the transverse oscillations vary from one fluid to the other. In the simulations, variations of Mo are achieved by varying Ga while keeping Bo constant. For each iso-Bo series (thin solid and dashed lines), St is seen to decrease with increasing Mo (hence, decreasing Ga). The reduced frequency approaches the threshold value, St_c, predicted by linear stability analysis (Bonnefis *et al.* 2024) at the maximum Mo at which path instability takes place at the considered Bo. This finding indicates that the presence of the wall does not affect the

oscillation frequency of bubbles close to the threshold of path instability. To check whether or not this is still the case further away from the threshold, we ran additional runs without the presence of the wall for (Bo, Ga) sets for which the NWZ evolution is observed when the wall is present. Comparing both sets of results reveals that interactions with the wall increase the reduced frequency for $Bo \geqslant 0.25$. For instance, with $Bo = 0.5$ and $Mo = 1.9 \times 10^{-9}$, St increases by nearly 20 % from the unbounded to the wall-bounded configuration. Some available experimental and numerical data, all of which were obtained in an unbounded fluid except those of Estepa-Cantero *et al.* (2024), are also included in the figure. These data are found to agree well with present predictions, confirming the accuracy of our simulations in the unbounded configuration (the low-Mo simulations of Cano-Lozano *et al.* (2016) suffer from under-resolution, which is why the data reported for $Mo = \mathcal{O}(10^{-10})$ slightly deviate from present predictions).

In the following sections, we examine in more detail the results corresponding to the three regimes that were not observed in Part 1, namely the BTE scenario which takes place at large enough Ga in the stable path regime, and the WMA and NWZ scenarios, which are both observed beyond the threshold of path instability.

4. The BTE regime

Figure 6 illustrates the evolution of several indicators for a bubble with $(Bo, Ga) = (0.05, 70)$ following a BTE evolution. According to panel (a), the bubble bounces twice before escaping from the near-wall region. Before each bounce, it first collides with the wall, as indicated by values of X_b (the distance from the bubble centroid to the wall) smaller than one. Upon collision, the aspect ratio quickly decreases to a minimum close to 1.0 and the bubble keeps this virtually spherical shape for approximately 3−4 time units (see the detailed evolution in panel b). Panels (c, d) show that, upon the second collision, the bubble rise velocity, V_y, falls dramatically by a factor of six, reducing from 4.8 at $T = 33$ to 0.75 at $T = 36.5$. Meanwhile, the direction of the wall-normal velocity, V_x, reverses three times. Between the last two reversals, V_x is negative, so that the bubble undergoes a short wall-ward migration prior to escaping definitively away from the wall region (mentioned as the 'Reversal' period in panel b).

Examination of the flow field in the vicinity of the bubble helps elucidate key aspects of the mechanisms involved. The inset in figure 6(e) shows the iso-contours of the spanwise vorticity component, $\overline{\omega}_z$, in the wall-normal symmetry plane $Z = Z_b$ just after the collision $(T = 36)$. This component is seen to be uniformly negative in the bubble vicinity, indicating that fluid particles experience a clockwise rotation about the Z-axis. The global rotation of fluid particles at the bubble surface may be quantified using the spinning rate $\overline{\boldsymbol{\Omega}}$ defined by (2.2). The evolution of its spanwise component, $\overline{\Omega}_z$, is illustrated in figures 6(e, f). Upon the first collision, $|\overline{\Omega}_z|$ quickly increases from zero to ≈ 1.4. Combined with the simultaneous sharp decrease of V_y, this suggests that part of the fluid kinetic energy associated with the bubble translation is converted into 'rotational' kinetic energy. The fluid surrounding the bubble being spinning, the bubble experiences a lift force $\boldsymbol{F}_L^{\mathrm{M}} \propto \overline{\boldsymbol{\Omega}} \times \boldsymbol{V}$, which may be interpreted as a Magnus-like force. As $\overline{\Omega}_z$, V_x and V_y are all of order unity during this transient stage, this force is expected to be comparable in magnitude to the buoyancy force. Since V_y is always positive, the wall-normal component of this force is positive, helping the bubble move away from the wall. This is the key mechanism that makes the BTE scenario possible. An essential characteristics of the Magnus-like force is that it keeps significant values over a long post-collision period of time, while the bubble has already moved a substantial distance away from the wall. For instance, figure 6(b) indicates that the gap is already one bubble radius

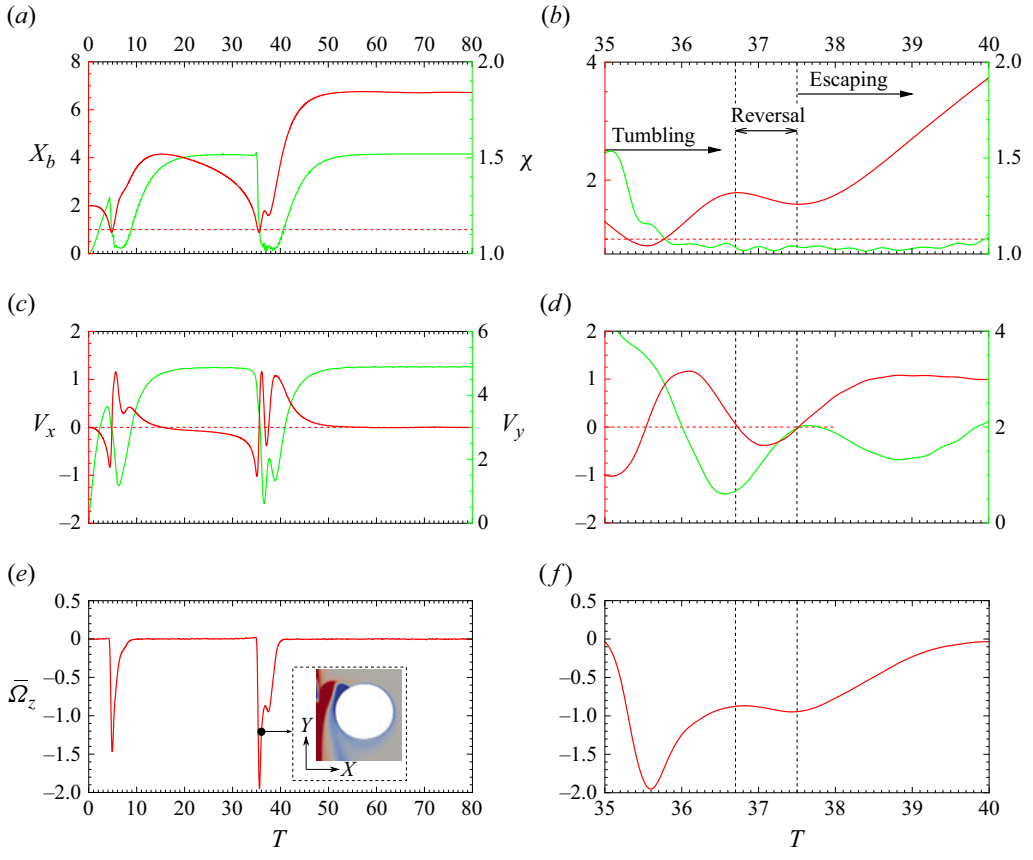

Figure 6. Evolution of several characteristics of the bubble motion during a BTE scenario for $(Bo, Ga) = (0.05, 70)$. The right panels provide a zoom of the evolution shown in the left panels in the time interval $35 \leqslant T \leqslant 40$. (a,b) show wall-normal bubble position (red line and left axis) and bubble aspect ratio (green line and right axis). (c,d) show wall-normal (red line and left axis) and vertical (green line and right axis) velocities of the bubble centroid. (e,f) show spinning rate of the bubble surface. The inset in panel (e) displays the iso-contours of the spanwise vorticity $\overline{\omega}_z$ at $T = 36$ in the symmetry plane $Z = Z_b$; red and blue colours refer to positive and negative values, respectively, with a maximum magnitude of 5.

wide $(X_b = 2)$ at $T = 38.3$, a moment at which, according to panels (d) and (f), the wall-normal component of $\overline{\boldsymbol{\Omega}} \times \boldsymbol{V}$ is still close to unity.

When V_x is positive, the vertical component $\boldsymbol{F}_L^{\mathrm{M}} \cdot \mathbf{e}_y$ is negative, thus counteracting buoyancy. This leads to a sharp decrease in V_y during the time interval $35.5 \leqslant T \leqslant 36.7$, and to a lesser extent from $T = 37.5$ to $T = 39$. Conversely, during the short wall-ward stage noticed for $36.7 \leqslant T \leqslant 37.5$, this component cooperates with the buoyancy force, resulting in an increase of the rise speed. Of course, viscous effects and liquid inertia play a central role beyond the transient stage during the Magnus-like force controls the bubble dynamics. Since near-wall dissipation increases as the gap shrinks, viscous processes are responsible for the sharp decrease of the rise speed prior to the collision $(33.5 \leqslant T \leqslant 35.5)$. Conversely, inertial effects associated with the amount of liquid displaced by the bubble result in an added-mass force that limits the time variations of V_y. This is why the rise speed is still only half its pre-collision value at $T = 40$, while $\overline{\Omega}_z$ has already almost returned to zero.

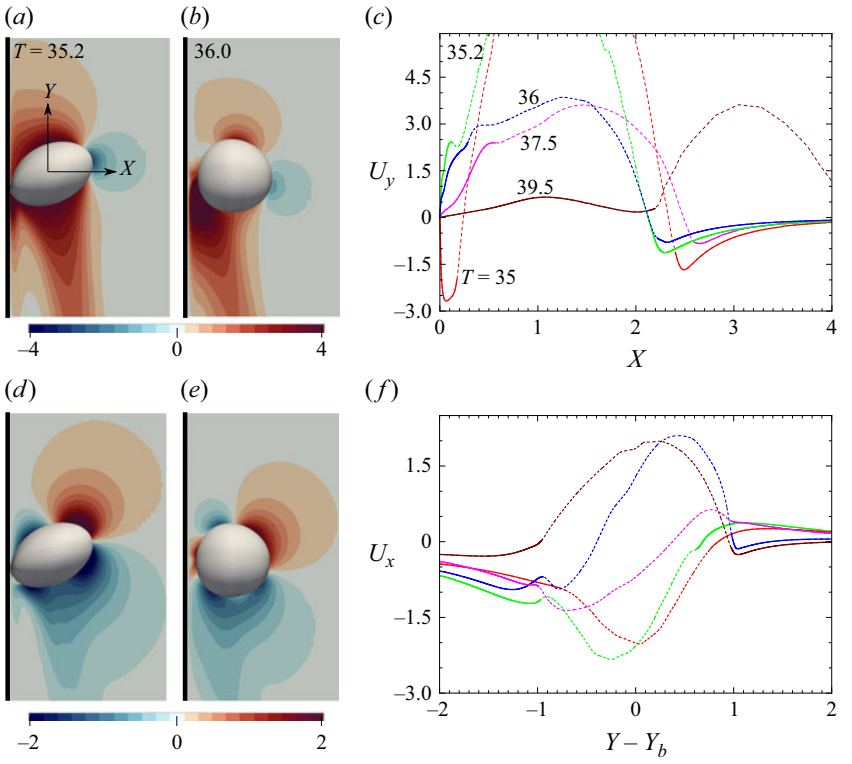

Figure 7. Evolution of the vertical (top row) and wall-normal (bottom row) fluid velocity in the vicinity of a bubble with $(Bo, Ga) = (0.05, 70)$. Panels $(a-b)$ and $(d-e)$ show the distribution in the wall-normal symmetry plane $Z = Z_b$ at $T = 35.2$ and 36, respectively. The bubble is rising upwards, and the wall is shown with a thick black line on the left. (c) Distribution of U_y along the horizontal line $Y = Y_b$, $Z = Z_b$, with solid and dashed lines showing the velocity outside and inside the bubble, respectively. (d) Same for U_x along the vertical line $X = X_b$, $Z = Z_b$.

The discussion above also helps explain the rapid variations noticed in the bubble shape upon the second collision, particularly the swift recovery of the spherical shape (see also figures 7$a-b$ and 7 $d-e$). This recovery is primarily driven by two factors. First, the significant decrease in the bubble rise speed immediately after the collision revealed by figure 6(d) reduces the pressure difference between the front stagnation point and the bubble's equator. As the bubble moves away from the wall, this quickly reduces its aspect ratio. Second, the strong collision-induced spinning flow around the bubble attenuates the local pressure differences in the fluid, maintaining its shape spherical for some time.

Figure 7 shows the bubble shape and position and the velocity distribution of the surrounding liquid in the symmetry plane $Z = Z_b$ just before and after the second collision. Panel (c) reveals that the extremum of U_y in the gap experiences an abrupt change from -2.6 at $T = 35$ to ≈ 2.5 at $T = 35.2$. The maximum U_y goes on increasing after the collision, reaching a value of 4.2 at $T = 36.5$ (not shown), before relaxing slowly to zero as the bubble moves away from the wall. The massive flow reversal in the gap at the beginning of the sequence results from the rapid decrease of the bubble rise speed, which forces fluid elements initially located in the wake to catch up with those located on both sides of the bubble and eventually replace them. The consequences of this catch-up process are milder along the fluid-facing side of the bubble, where the negative vertical velocity is significantly reduced but does not change sign over an $\mathcal{O}(1)$-thick fluid layer. The positive

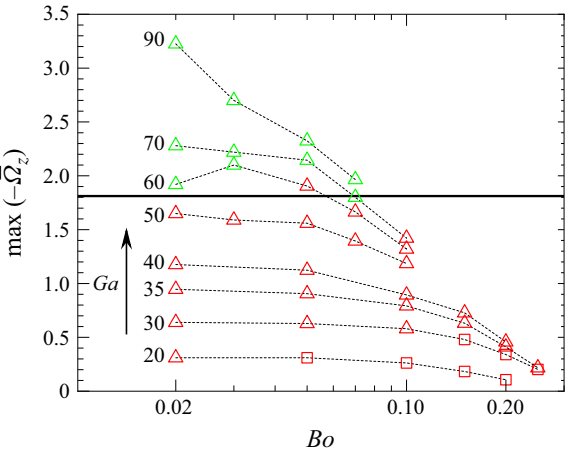

Figure 8. Variation of the maximum spinning rate with the Bond and Galilei numbers. Symbols are identical to those in figure 2. The thick horizontal line corresponds to $max(|\overline{\Omega}_z|) = 1.8$.

U_y in the gap and their negative counterpart on the fluid-facing side both provide negative contributions to the z-component of the cross product $(\mathbf{X} - \mathbf{X}_b) \times \mathbf{U}$ at the bubble surface, hence to $\overline{\Omega}_z$. However, the contribution coming from the gap is $3-4$ times larger, and the difference is even larger before the collision, owing to the weak negative values of U_y on the fluid-facing side ($U_y \approx 0$ at the position where the solid green line corresponding to $T = 35.2$ turns dashed). Owing to the predominant suction of the wake towards the gap region, the wall-normal velocity is negative at the back of the bubble, as panels $(d-e)$ confirm. These negative U_x values are significantly larger than their positive counterpart ahead of the bubble (see panel f), providing another sizeable negative contribution to $\overline{\Omega}_z$.

The BTE regime may set in only if the spinning rate resulting from the mechanism described above is strong enough. Figure 8 displays the maximum spinning rate computed along the bubble path for all cases corresponding to a periodic bouncing or a BTE regime; some cases with $Ga \leqslant 30$ considered in Part 1 are also included. Simulations corresponding to $40 \leqslant Ga \leqslant 70$ where run with an initial separation $X_0 = 3.5$, to ensure that the possible escape event takes place after the first collision (see Appendix B for a discussion of the influence of X_0 on the escape process). These results suggest that the bubble path transitions from the periodic bouncing regime to the BTE regime when the maximum spinning rate exceeds a critical value close to 1.8.

To get some more insight into the magnitude of the Magnus-like force, an estimate of the other transverse forces acting on the bubble during its escape from the wall region is required. Some of the kinematic data provided in panels (b),(d) and (f) of figure 6 may be used for this purpose, noting that the bubble remains nearly spherical in the time interval $36 \lesssim T \lesssim 40$, as panel (b) indicates. Consider for instance the situation at $T = 37.5$, a moment at which the transverse velocity, V_x, hence the transverse quasi-steady viscous drag force, is zero. At this moment, $X_b \approx 1.6$, $V_y \approx 2.0$, $\overline{\Omega}_z \approx -0.95$. Once normalised by $\rho_l g R^3$, the Magnus-like force may be written in the form $\boldsymbol{F}_L^{\mathrm{M}} = (4/3)\pi C_L^{\Omega} \overline{\boldsymbol{\Omega}} \times \boldsymbol{V}$, with C_L^{Ω} being the (unknown) Magnus lift coefficient. Hence, the wall-normal component of this force at this position is approximately $7.95 C_L^{\Omega}$. At the same transverse position, the attractive force $\boldsymbol{F}_P = -(\pi/2) C_P V_y^2 \mathbf{e}_x$ resulting from the Bernoulli effect is close to -0.38, based on the estimate of the interaction coefficient $C_P(X_b = 1.6) \approx 0.06$ resulting from equation 7 of Takemura & Magnaudet (2003). As discussed in Part 1, there is a

large uncertainty in the magnitude of the transverse component of the inertia-induced force, owing to the unknown contribution of the trailing vortices entrained laterally by the bubble. With all due caution, an order-of-magnitude estimate of this force may be obtained by neglecting this contribution. With this assumption, the transverse inertia-induced force, $\boldsymbol{F}_I \cdot e_x = -(4/3)\pi C_I \mathrm{d}V_x/\mathrm{d}T$ may be estimated by simply considering that the inertia-induced coefficient, C_I, is close to the familiar added-mass coefficient of a sphere accelerating in an unbounded fluid, i.e. $C_I \approx 1/2$. With $\mathrm{d}V_x/\mathrm{d}T \approx 1.45$ at $T = 37.5$, this estimate yields $\boldsymbol{F}_I \cdot \mathbf{e}_x \approx -3.04$, suggesting that this contribution dominates the overall force that resists the bubble escape. Summing the two resistive contributions and assuming that the repulsive Magnus-like force is almost in balance with the overall attractive force implies $C_L^{\Omega} \approx 0.43$. A similar estimate may be performed at $T = 38.3$, a moment when the gap thickness equals the bubble radius ($X_b = 2.0$), so that $C_P \approx 0.024$. At this moment, $V_x \approx 1.0$, $V_y \approx 1.6$, $\overline{\Omega}_z \approx -0.6$ and $\mathrm{d}V_x/\mathrm{d}T \approx 0.8$, which yields $\boldsymbol{F}_P \cdot \mathbf{e}_x \approx -0.1$ and $\boldsymbol{F}_I \cdot \mathbf{e}_x \approx -1.68$. At this position, the Reynolds number $Re = 2Ga(V_x^2 + V_y^2)^{1/2}$ is close to 265, making it possible to estimate the quasi-steady transverse drag force using Moore's high-Reynolds-number prediction (Moore 1963). In the present notations, this yields $\boldsymbol{F}_D \cdot \mathbf{e}_x \approx -12\pi(1 - 2.2Re^{-1/2})Ga^{-1}V_x \approx -0.47$. Adding all three attractive contributions together and balancing with the Magnus-like force now implies $C_L^{\Omega} \approx 0.56$. The above two predictions for the Magnus lift coefficient, corroborated by similar estimates for other (Bo, Ga) sets, suggest that $C_L^{\Omega} \approx 0.5 \pm 0.07$. Although this result is reminiscent of the well-known inviscid prediction for the lift coefficient C_L^s of a sphere immersed in a weak linear shear flow, $C_L^s = 1/2$, this is presumably largely coincidental given the very different nature of the present conditions, in which unsteadiness, flow inhomogeneity and wall vicinity play a central role.

5. Regimes encountered beyond the path instability threshold

5.1. *The WMA regime*

The first phenomenology encountered beyond the neutral curve, at least up to $Ga = 90$, corresponds to the WMA regime. To illustrate this regime, we select a bubble with $(Bo, Ga) = (1.5, 50)$, i.e. a Morton number $Mo = 5.4 \times 10^{-7}$, close to that of silicone oil DMS-T05. According to figure 2(*a*), the associated conditions are by far supercritical, since the critical Bond number for this specific liquid is close to 0.85.

Figure 9 shows how the characteristics of the path and geometry of this bubble evolve as it rises. Panels $(a-b)$ indicate that path instability quickly sets in and saturates after a few cycles of oscillations. Path oscillations take place in the wall-normal plane and give rise to a planar zigzagging motion, since the horizontal wall-parallel velocity component, V_z, remains vanishingly small throughout the bubble ascent. At the same time, the bubble gradually migrates away from the wall with, according to panel (*a*), an average drift velocity close to 0.01, much smaller than the maximum of V_x, which is close to 0.4. The evolution of this velocity component is far from being perfectly sinusoidal, indicating that the dynamics of the zigzagging motion is nonlinear. This nonlinearity is further highlighted in panel (*c*), which shows the evolution of the transverse and vertical accelerations. In particular, the time record of $\mathrm{d}V_x/\mathrm{d}T$ exhibits small oscillations with a frequency five times larger than that of the primary oscillations. The vertical velocity also exhibits strongly non-sinusoidal oscillations which make the bubble rise speed vary upon time by 7.5 %. According to panel (*b*), the primary oscillations of V_x have a frequency $\overline{f} = 0.092$, in perfect agreement with the predictions of the linear stability analysis performed by Bonnefis *et al.* (2024) with a deformable bubble rising in an unbounded fluid

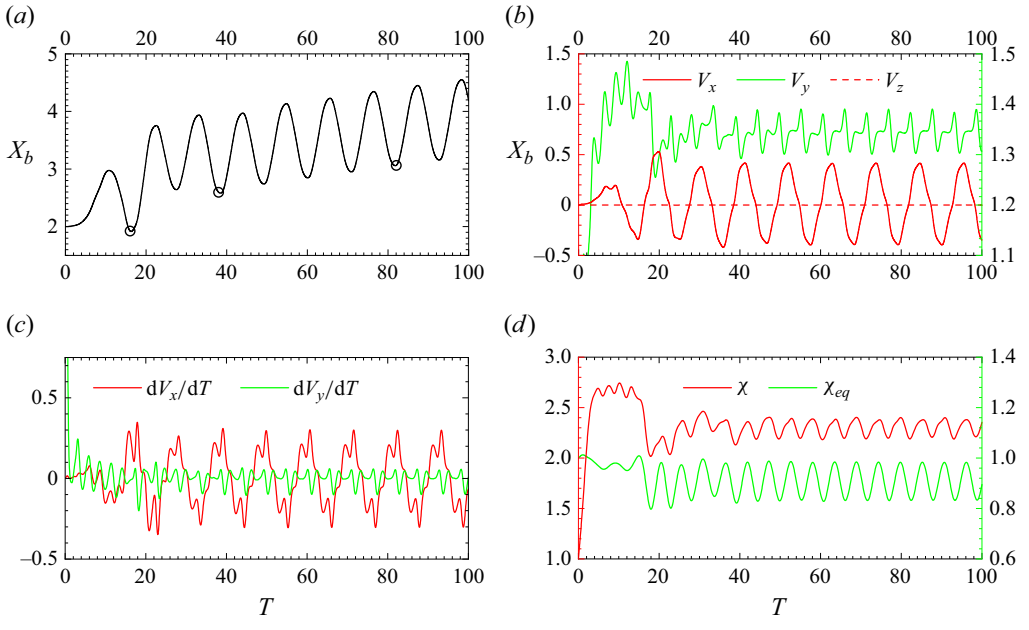

Figure 9. Evolution of various characteristics of the bubble path and geometry during the lateral migration of a bubble with $(Bo, Ga) = (1.5, 50)$. (*a*) Wall-normal position of the centroid; (*b*) wall-normal (solid red, left axis), horizontal wall-parallel (dashed red, left axis) and vertical (solid green, right axis) components of the bubble centroid velocity; (*c*) wall-normal (red) and vertical (green) acceleration of the centroid; (*d*) principal bubble aspect ratio (red, left axis) and equatorial axes ratio (green, right axis). The three circles in (*a*) identify the first three moments at which the wake structure is shown in figure 10.

(see their figure 10*b*). The same study revealed that a secondary mode becomes unstable when Bo exceeds the critical value 1.38 (their figure 10*a*). This mode corresponds to axisymmetric shape oscillations about the bubble minor axis (so-called (2, 0) oscillatory mode for oblate spheroids). The predictions of Bonnefis *et al.* (2024) indicate that, for $(Bo, Ga) = (1.5, 50)$, the frequency of these shape oscillations is 5.5 larger than that of path oscillations, close to the ratio of five noticed in panel (*c*). This proximity strongly suggests that the high-frequency oscillations present in the evolutions of the velocity and acceleration components in figure 9 are the footprint of this mode of shape oscillations.

Besides these small-amplitude high-frequency oscillations, figure 9(*d*) makes it clear that the bubble undergoes significant periodic shape variations along its path. Both the principal aspect ratio, χ, and the equatorial axes ratio, χ_{eq}, reach their minimum at the extremities of each zigzag, where V_x vanishes and $\mathrm{d}V_x/\mathrm{d}T$ reaches its extrema. These simultaneous variations indicate that the bubble experiences a periodic compression/dilatation along the equatorial axis lying in the wall-normal plane (the x'-axis with length b in figure 1*b*). Examination of bubble contours in the appropriate planes (not shown) reveals that these variations are accompanied by simultaneous phase-opposed oscillations along the z'-equatorial axis, while the bubble keeps an almost constant length along the y'-minor axis. Therefore, the observed changes in χ and χ_{eq} appear to be driven by pressure variations whose wavelength is half the perimeter of the bubble contour lying in the equatorial (x', z')-plane. These oscillations are induced by (and enslaved to) the transverse motion of the bubble. So, their dynamics is distinct from that of natural shape oscillations of bubbles rising in a straight line, as underlined by their much smaller frequency. Note that the wall plays no role in this dynamics, since the figure

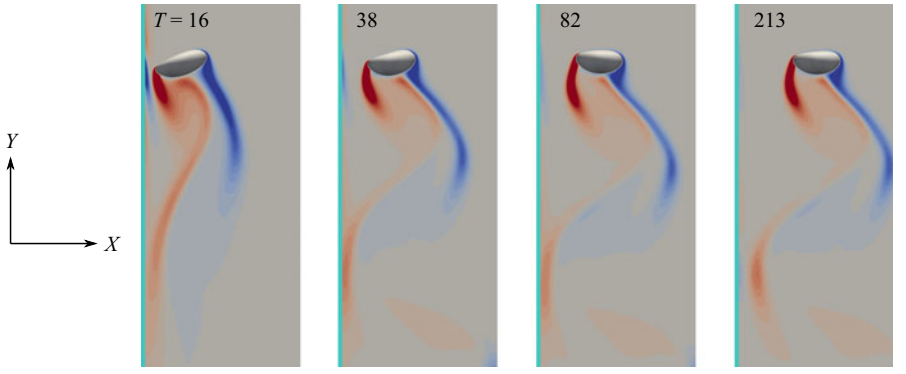

Figure 10. Distribution of the spanwise vorticity, $\overline{\omega}_z$, in the symmetry plane $Z = Z_b$ past a bubble with $(Bo, Ga) = (1.5, 50)$ at several moments when it reaches the wall-facing extremity of a zigzag (circles in figure 9*a*). Red and blue iso-contours refer to positive and negative values of $\overline{\omega}_z$, respectively, with a maximum magnitude of 2.0.

makes it clear that the minima reached by χ and χ_{eq} are identical at both ends of a given zigzag, i.e. they do not depend on the instantaneous wall-normal position of the bubble. In addition to these zigzag-driven oscillations, the bubble shape exhibits a marked asymmetry along the x'-axis, with its vertical cross section taking an egg-like shape pointing towards the exterior of the zigzag (see figure 10).This asymmetry is not related to the presence of the wall. Rather, as analysed by Cano-Lozano *et al.* (2016), it results from the periodic rotation of the bubble about the z'-axis, which lowers (increases) the pressure on the part of the surface located the farthest from (the closest to) the zigzag centreline.

Figure 10 shows how the distribution of the spanwise vorticity evolves as the bubble moves progressively away from the wall. The four snapshots are taken at moments when the bubble reaches the wall-facing extremity of a zigzag. A wall layer with significant $\overline{\omega}_z$-values is present, even ahead of the bubble, at $T = 16$, with in particular a stripe of intense negative vorticity (corresponding to a downstream flow) in the bubble–wall gap. This structure still subsists at $T = 38$, albeit with a much weaker intensity, and disappears in later times. Only in the downstream region located several radii downstream of the bubble do significant non-zero values of $\overline{\omega}_z$ subsist close to the wall. This is where the wake still weakly interacts with the wall, generating a small repulsive force responsible for the average migration through the familiar vortical mechanism summarised in § 1 and already active in finite-to-moderately inertial regimes. To summarise, apart from the early stages of the rise, present observations only detect weak interactions of the wake with the wall, and reveal a close agreement with the global stability predictions of Bonnefis *et al.* (2024) in an unbounded fluid regarding the characteristics of the zigzagging motion. Combining both aspects leads us to the conclusion that the WMA regime consists essentially of the superposition of the oscillating path resulting from the path instability mechanism in an unbounded flow (with the wall only dictating the orientation of the symmetry plane of the path), and the gradual wake-induced migration away from the wall already active at lower Ga, especially with moderately deformed bubbles (see figure 16). The same conclusion holds in the WMA scenario observed with spiralling bubbles. In particular, we examined the path and dynamics of a bubble with $(Bo, Ga) = (2, 60)$ rising in silicone oil DMS-T05 and found that once its wake, made of a pair of vortex threads wrapped around one another, is fully developed, it only weakly interacts with the wall in a manner similar to that displayed in figure 10.

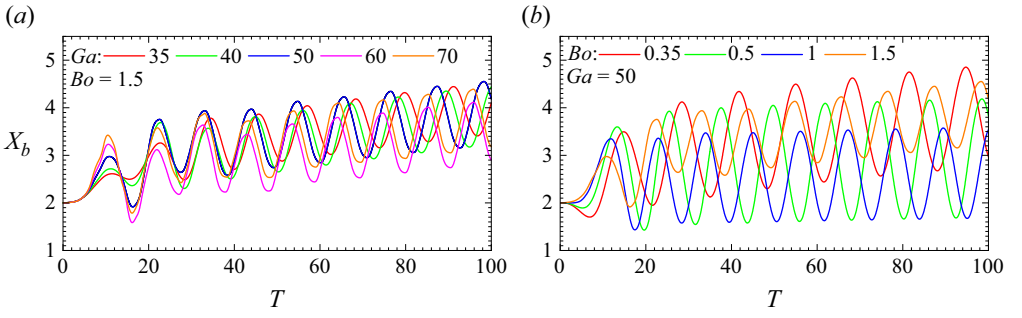

Figure 11. Influence of the Bond and Galilei numbers on the evolution of the wall-normal position of the bubble centroid in the WMA regime. (*a*) Increasing Ga at fixed Bo; (*b*) increasing Bo at fixed Ga.

Figure 11 gathers some records of the bubble path for various Ga at $Bo = 1.5$ (panel *a*), and for various Bo at $Ga = 50$ (panel *b*). Clearly, the average velocity with which the bubble migrates away from the wall varies non-monotonically with the control parameters in both cases. For instance, the fastest migration in panel (*a*) is seen to be reached for $Ga = 50$ (blue curve), while the slowest one is obtained for $Ga = 60$ (purple), with the two evolutions corresponding to $Ga = 40$ (green) and 70 (orange) exhibiting intermediate migration velocities. Noting that in the saturated stage the amplitude of the zigzagging motions experiences little variation with Ga, it appears that the early stages of the path are responsible for the most part of the non-monotonic variations of the average migration velocity. For a fixed Bo, the higher Ga the larger the growth rate of the zigzagging motion, since increasing Ga increases the distance to the path instability threshold. For this reason, the transverse oscillations of paths corresponding to $Ga = 60$ and 70 quickly reach a large amplitude, which, at the end of the first cycle of oscillations, brings the bubbles closer to the wall than at the time of their injection (e.g. $X_b \approx 1.6$ at $T = 16$ for $Ga = 60$). Taking the bubble with $Ga = 35$ as reference, this induces a delay in the average migration of bubbles with a higher Ga that is never caught up in later stages. Similarly, when Ga is kept fixed and Bo is increased, the bubble closest to the path instability threshold ($Bo = 0.35$, red line in panel *b*) quickly reaches average distances from the wall larger than bubbles with $Bo = 0.5$ (green) and $Bo = 1$ (blue), whose zigzags amplitude grows faster. However, at saturation, these amplitudes greatly vary with the Bond number, i.e. with the bubble shape, passing through a maximum for $Bo = 0.5$ (see § 5.3 for more discussion on this aspect). As a result of this marked variation, the amplitude of the zigzags performed by the bubble with $Bo = 0.5$ is twice as large as that of the bubble with $Bo = 1.5$. This is why the latter migrates faster than those with $Bo = 1$ and 0.5 which spend more time close to the wall throughout their ascent.

5.2. *The NWZ regime*

Figure 2(*a*) indicates that, beyond the neutral curve but some distance away from it, bubbles with $Ga \gtrsim 60$ and $Bo \lesssim 1$ follow a NWZ scenario. Figure 12 illustrates the evolution of some characteristics of the dynamics of two such bubbles. The main difference between the two evolutions is the occurrence of direct bubble–wall collisions in the former case. Collision events can be identified from the temporal evolution of the dimensionless gap, $\overline{\delta}$. In line with the definition recalled in § 2, we consider that a direct collision takes place when $\overline{\delta}$ becomes less than the minimum cell size, $\overline{\Delta}_{min}$, such as during the first event displayed in the inset of figure 12(*a*). As this figure shows, $\overline{\delta}$ decreases to $\overline{\Delta}_{min}$ at regular time intervals, first at $T \approx 18$. In all NWZ evolutions

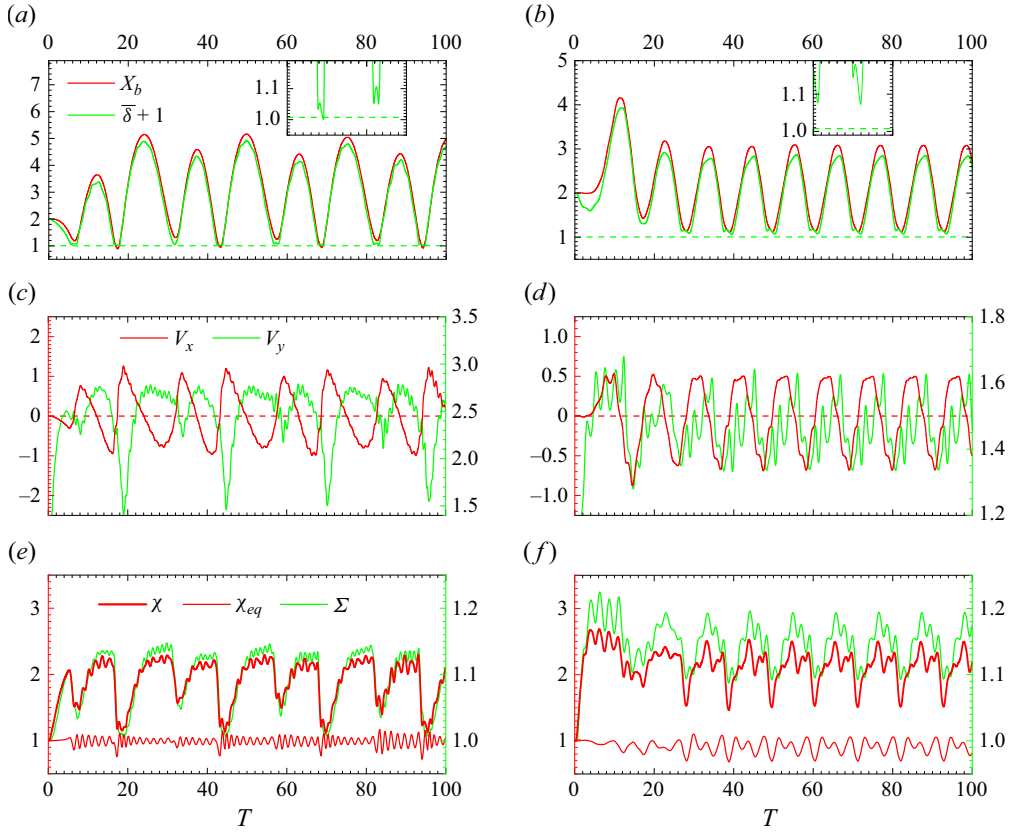

Figure 12. Evolution of some characteristics of the bubble dynamics for $(Bo, Ga) = (0.25, 90)$ (left column) and $(1, 70)$ (right column). (a,b) Wall-normal position of the bubble centroid (red line) and gap thickness (green line); (c,d) wall-normal (red) and vertical (green) components of the velocity of the bubble centroid; (e,f) principal aspect ratio (thick red line), equatorial axes ratio (thin red line) and surface area (green line). In $(c-f)$, the right axis refers to the quantity shown with the green line. In $(a-b)$, the insets are located at the actual position on the horizontal (time) axis and only their vertical axis is stretched; the green dashed line identifies the transverse position $1+\overline{\Delta}_{min}$.

involving collisions, these events occur every other round of transverse oscillations. Upon collision, V_x reverses and peaks at an absolute value larger than that achieved prior to the collision (see panel c), which may be interpreted as a rebound with a restitution coefficient larger than one. Consequently, the maximum separation reached by the bubble in the upcoming zigzag is significantly larger than that achieved just before the collision. In contrast, when collisions do not take place, the maximum separation remains constant once the oscillations have saturated (see panel b), and the restitution coefficient is smaller than one throughout the bubble ascent. Collisions also deeply affect the evolution of the bubble rise speed. As panel (c) shows, this component reduces by nearly 50 % shortly after the collision ($V_y \approx 1.5$). In contrast, this reduction reaches only 20 % in the next zigzagging cycle during which no collision takes place, and the same observation holds for the second bubble that never collides with the wall (panel d). In addition to these dominant variations enslaved to the zigzag dynamics, V_y also exhibit fast small-amplitude oscillations, especially in the case of the bubble with the smallest Bo. Qualitatively similar evolutions are noticed in panels $(e-f)$ for the principal aspect ratio χ, and the surface area Σ (defined as the area of the gas–liquid interface normalised by $4\pi R^2$).

These results reveal the existence of two distinct modes of shape oscillations: a primary low-frequency mode, by which χ and Σ reach their maximum (respectively, minimum) when the bubble–wall separation achieves its maximum (respectively, minimum), and a secondary high-frequency mode with a significantly smaller amplitude. This second mode is seen to dominate the time variations of the equatorial axes ratio χ_{eq}, whose relative magnitude is up to 20 % in the stages when the bubble is 'far' from the wall.

We compared the frequency of this second mode with that of small-amplitude capillary oscillations in the inviscid limit. For a nearly spherical bubble, the fundamental mode of such oscillations has a frequency $\overline{f}_2 = \sqrt{12}Bo^{-1/2}$ (Lamb 1932). Increasing the bubble oblateness leads to a decrease in this frequency, as the nonlinear computations of Meiron (1989) showed. The two deformable bubbles considered in figure 12 have a principal aspect ratio $\chi \approx 2.1$. For this oblateness, Meiron's predictions indicate that the frequency of the lowest-order axisymmetric oscillations (corresponding to the (2, 0) mode) is $\approx 0.84\overline{f}_2$. However, variations observed in panels $(e-f)$ on the equatorial axes ratio χ_{eq} prove that the observed high-frequency oscillations are three-dimensional. The lowest two three-dimensional capillary modes are the (2, 1) and (2, 2) ones, the wavelength of which in the equatorial plane is the corresponding perimeter and half of it, respectively. Meiron's results predict that, for an oblate spheroid with $\chi = 2.1$, their frequencies are approximately $0.81\overline{f}_2$ and $0.56\overline{f}_2$, respectively. Inspection of the records of χ_{eq} in panels $(e-f)$ indicates that the frequency of the observed high-frequency oscillations is close to $0.59\overline{f}_2$ at $Bo = 0.25$ and $0.50\overline{f}_2$ at $Bo = 1$. Given that the rise Reynolds number in the second case is less than half that in the first one, viscous corrections are expected to be more significant in the former. With this in mind, this comparison strongly suggests that the observed oscillations correspond to the non-axisymmetric (2, 2) mode for both bubbles.

To better quantify wall effects, we carried out additional runs considering the same two bubbles in an unbounded domain. After exhibiting flattened spiralling paths, they both eventually describe planar zigzags with reduced frequencies $St = 0.057$ and $St = 0.113$ for $(Bo, Ga) = (0.25, 90)$ and $(1, 70)$, respectively. These frequencies are slightly smaller than their wall-bounded counterparts ($St = 0.063$ and 0.126, respectively). However, the most prominent difference is that shape oscillations keep a much smaller amplitude in the absence of the wall. This difference is highlighted in figure 13, which shows the variation over a single zigzag period of the velocity components of the bubble centroid and its surface area as a function of the lateral displacement, $X_b - X_c$, with X_c being the time-averaged wall-normal position of the centroid, i.e. the horizontal position of the zigzag centreline. In the unbounded configuration, the two halves of the zigzag period exhibit symmetric evolutions with respect to the mean position $X = X_c$. For both bubbles, the relative change in Σ remains less than 3 % throughout the zigzag period, indicating weak shape oscillations. In the presence of the wall, the mean amplitude of the lateral oscillations is reduced by 20 %–25 % and no symmetry with respect to $X = X_c$ subsists. The bubble surface area experiences marked variations, with relative changes from 10 % to 15 %. For both bubbles, Σ attains its minimum shortly after the bounce, making the bubble less deformed during most of the departing stage than when it recedes to the wall.

Figure 14 visualises the wake structure downstream of the bubble with $(Bo, Ga) = (0.25, 90)$ using the λ_2 criterion (Jeong & Hussain 1995). In the unbounded case (panels a, b), this structure corresponds to the '4R' vortex shedding mode, following the terminology of Horowitz & Williamson (2010). This mode refers to two pairs of counter-rotating vortices with opposite signs of $\overline{\omega}_y$ successively shed in the wake during a zigzag half-period, with one pair being much stronger than the other, thus allowing the path to remain almost sinusoidal. The '4R' mode is known to be linked to oscillations in the

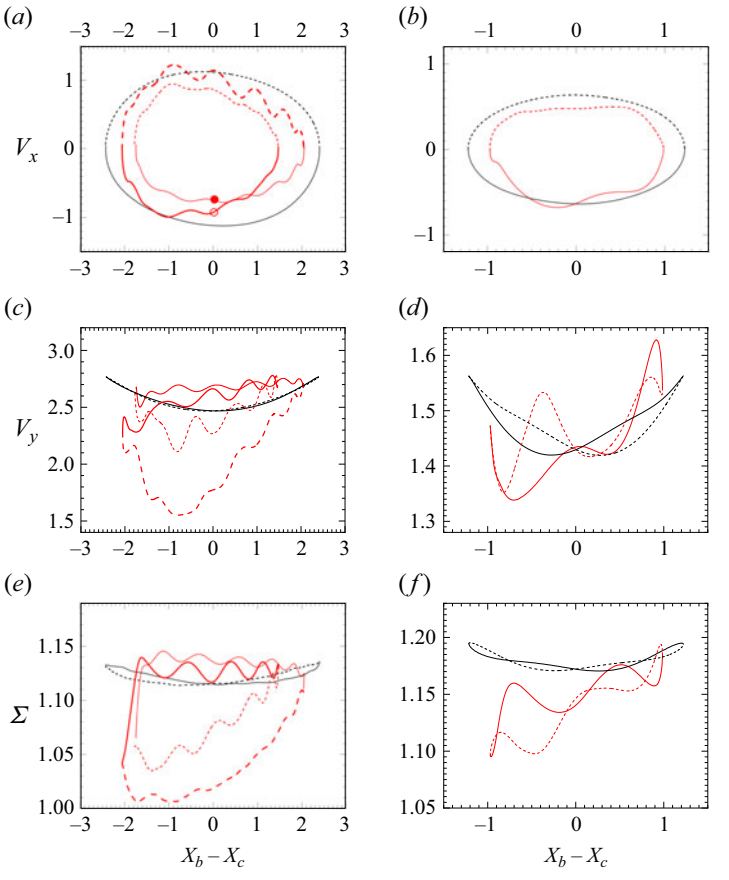

Figure 13. Variation of several characteristics of the bubble dynamics over a single zigzag period in the presence or absence of a wall for two bubbles with $(Bo, Ga) = (0.25, 90)$ (left column) and $(Bo, Ga) = (1, 70)$ (right column). (a,b) Horizontal velocity component, V_x, lying in the plane of the zigzagging motion (i.e. wall-normal component when the wall is present); (c,d) vertical velocity, V_y; (e, f) surface area, Σ. Red and black lines denote results in the presence and the absence of the wall, respectively. Solid and dashed lines refer to the half-period of the zigzag with negative and positive V_x, respectively; thick and thin red lines correspond to the sub-period of the zigzag with and without a collision, respectively.

relative velocity between the body and fluid (here the bubble rise speed). It emerges when the relative magnitude of these oscillations (with reduced frequency $2St$) exceeds approximately 10 % (Horowitz & Williamson 2010; Cano-Lozano *et al.* 2016; Auguste & Magnaudet 2018), a condition widely fulfilled in the present case according to figure 12(c). In the wall-bounded configuration (panels $c-f$ in figure 14), the vortex pair shed towards the wall degenerates into a short series of vortex patches, creating a strong suction effect on the bubble in the early departure stage. This is the cause of the sharp decrease in the bubble rise speed and surface area during this stage. The wall effect is less severe in cases where collisions do not happen, such as the bubble with $(Bo, Ga) = (1, 70)$ (not shown). In such cases, the wall compels the same vortex pair to bend and align vertically but the corresponding primary vortices do not break into distinct patches.

The structure of the vortex pair shed towards the fluid interior differs significantly from that in the unbounded configuration. Specifically, several single-sided, short-wavelength loops superimpose onto the primary vortex pair (panels c, e in figure 14). These loops grow in time and progressively invade the far-wake structure. Close inspection indicates

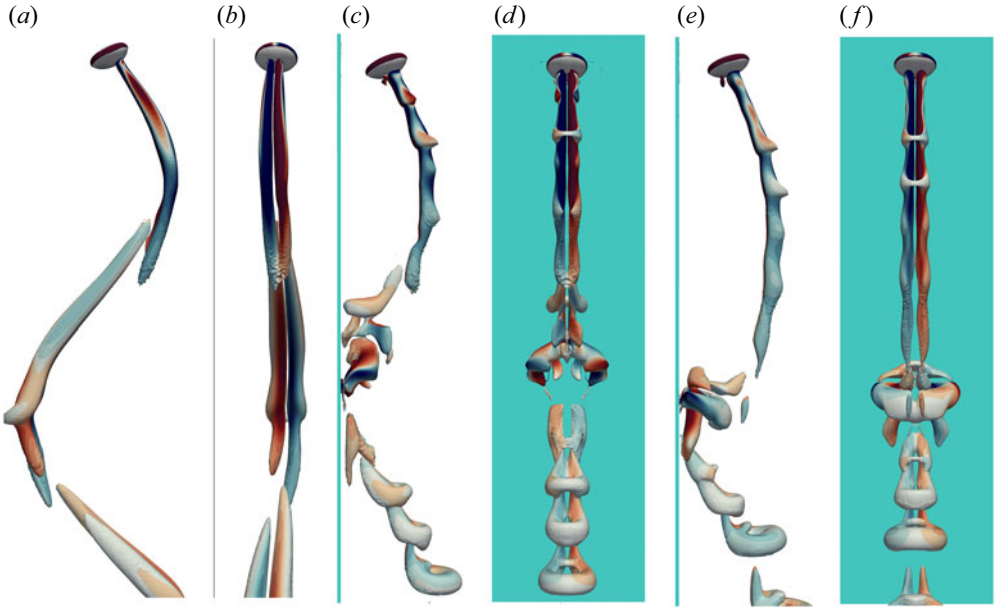

Figure 14. Two perpendicular views of the wake structure past a zigzagging bubble with $(Bo, Ga) = (0.25, 90)$ at the moment when the bubble crosses the centreline of the zigzag. $(a-b)$ Unbounded configuration; $(c-f)$ wall-bounded configuration. Snapshots in panels $(c-d)$ and $(e-f)$ are taken at the instants of time marked with open and closed circles in figure 13(a), respectively. The wake structure is visualised using the λ_2 criterion, with iso-λ_2 surfaces coloured by the local value of $\overline{\omega}_y$; red and blue contours refer to positive and negative values, respectively, with a maximum magnitude of 1.0. The wall is indicated by a dark green line in (c,e) and a dark green rectangular surface in (d,f).

that their number matches that of the high-frequency oscillations of the bubble aspect ratio, suggesting that these short-wavelength loops are a by-product of shape oscillations. Indeed, every transient change in the bubble shape (especially in the vicinity of the bubble's equator) results in a change in the local curvature of the bubble surface, hence in a variation of the magnitude of the tangential surface vorticity (Veldhuis *et al.* 2008; Cano-Lozano *et al.* 2016). The lifetime of these short-wavelength loops depends on the oscillatory Reynolds number, $Re_{osc} = (\rho_l \gamma R)^{1/2}/\mu_l = Ga\, Bo^{-1/2}$, that compares the characteristic time of shape oscillations with that of their viscous damping. Hence, when the Bond number is low enough, these oscillations decay slowly and are able to alter significantly the far-wake structure.

5.3. *How a zigzagging bubble gets trapped near the wall*

That the NWZ regime is encountered in an intermediate range of Bond numbers for $Ga \geqslant 60$ is somewhat surprising at first glance. Indeed, at a given Ga, bubbles with a slightly subcritical Bo migrate away from the wall and those whose Bond number exceeds 1.5 do the same through the WMA scenario (figure 2a). The reduced deformation of the bubble in the departing stage of the zigzagging motion revealed by figures 13(e,f), which itself results from the reduction in the rise speed induced by the intense interaction of the wake vortices with the wall (figures 14$c-f$), is responsible for the observed trapping phenomenon. Indeed, since the minor and major axes of an oblate spheroid vary as $\chi^{-2/3}$ and $\chi^{1/3}$, respectively, the frontal area of the bubble involved in the transverse motion, say $S_\perp$, varies as $\chi^{-1/3}$. Thus, it is larger when the bubble moves away from the wall

with $\chi \approx 1$ than when it goes back to it with $\chi > 2$. Throughout the departing stage, this results in an increase in the transverse viscous drag (for a given wall-normal velocity), as well as in the amount of liquid displaced transversely by the bubble, hence the transverse added-mass force (for a given wall-normal acceleration). Both effects tend to oppose the departing motion of the bubble. Therefore, the larger the frontal area $S_\perp$, the weaker the positive transverse velocity V_x the bubble can achieve at a given wall-normal position X_b. This is why, as figure 13 highlights, the amplitude of the zigzags, i.e. the horizontal distance between two successive V_x-reversals, is reduced compared with that achieved by the same bubble in an unbounded fluid. Moreover, in the highly inertial regime under consideration, the repulsive interaction force is known to vary approximately as $X_b^{-4}V_y^2$ for a nearly spherical bubble (Takemura & Magnaudet 2003). Although bubbles concerned by the NWZ regime are far from spherical, this scaling provides a strong indication that the dramatic reduction in the rise speed during the first half of the departing stage leads to a drastic drop in the repulsive force. Both aspects cooperate to hamper the drift of the wall-normal position of the zigzag centreline, X_c, yielding a near-wall trapping of the bubble from which the observed periodic path ensues.

Figure 15(a) illustrates the variations of the bubble area, Σ, with the wall distance over one zigzag pseudo-period for bubbles with $Bo = 0.5$ at different Ga. With no surprise, Σ experiences negligible changes at $Ga = 40$, the critical Ga at which path instability sets in at this specific Bond number. These variations become discernible at $Ga = 50$ but the bubble still manages to escape from the wall region. The surface area is seen to experience much larger changes (of the order of $7\,\% - 8\,\%$) for $Ga \geqslant 60$. Figure 2(a) indicates that this corresponds to the Ga-range in which the NWZ regime is observed for $Bo = 0.5$, which is in line with the physical arguments presented above. Figure 15(b) shows how the contour of the bubble in the diametrical plane perpendicular to the transverse motion varies along the departing and approaching stages at a given Ga. These plots confirm that this cross section is significantly less oblate in the departing stage for $Ga > 50$. The relative difference in the corresponding frontal area between the two stages becomes more pronounced as Ga increases further. This difference increases with Ga, i.e. with the distance to the threshold of path instability, and is approximately $8\,\%$ at $Ga = 90$. Figures 15(c,d) show results similar to those in the previous two panels for bubbles with $Ga = 70$ over a wide range of Bond number. Almost no change in either Σ or $S_\perp$ is noticed at $Bo = 0.2$, the critical Bo at which path instability sets in at this specific Galilei number. The situation changes drastically when the Bond number increases up to 0.25, with now a relative difference of around $15\,\%$ in $S_\perp$ between the approaching and departing stages. Then, this difference reduces gradually as Bo goes on increasing. The NWZ regime subsists up to $Bo = 1$ and is succeeded by the WMA regime at $Bo = 1.5$, where Σ and $S_\perp$ both experience negligible variations.

As pointed out above, the NWZ regime is a consequence of the intense interaction of the wall with the double-threaded wake accompanying zigzagging bubbles. Therefore, for this regime to exist, it is necessary that the lateral excursions performed by the zigzagging bubble have a sufficient amplitude. Given the supercritical nature of path instability (Mougin & Magnaudet 2002), the required amplitude may only be reached if Bo is somewhat larger than $Bo_c(Ga)$, the critical Bond number corresponding to the onset of the zigzagging motion at the considered Ga. This is why bubbles with Bo only slightly above Bo_c are still able to migrate away from the wall. The reason for the existence of a maximum Bo for the NWZ regime is somewhat more subtle. As is well known, zigzagging bubbles rise in such a way that their minor axis remains almost aligned with their path at all times (Ellingsen & Risso 2001; Mougin & Magnaudet 2006). For this,

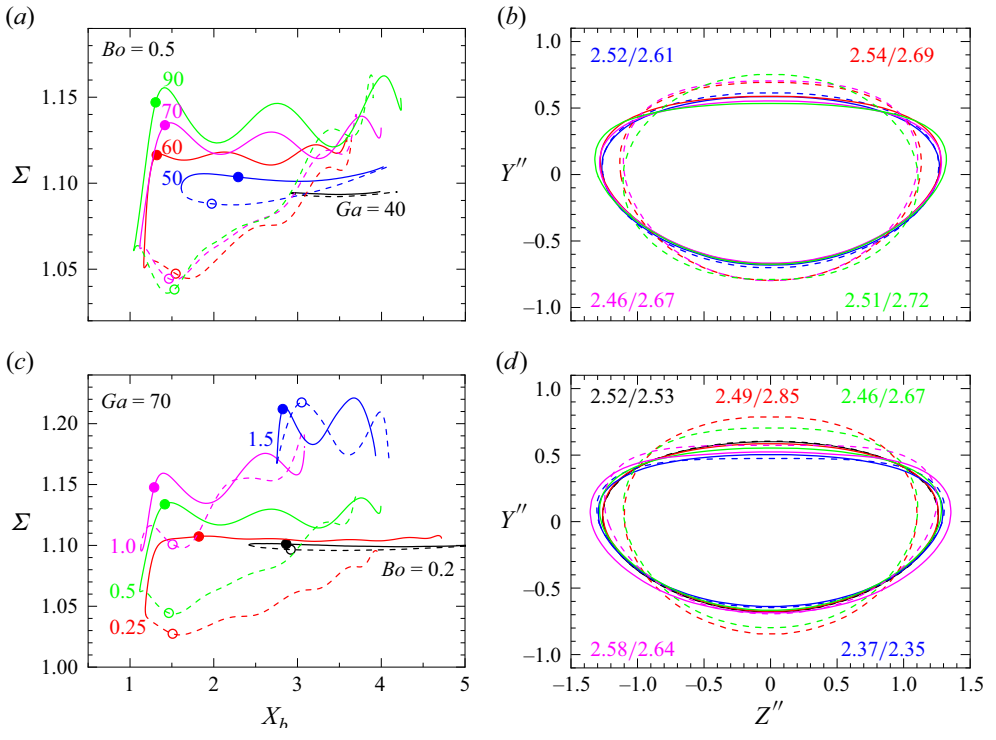

Figure 15. Time-dependent deformation of bubbles obeying a NWZ or a WMA scenario. (a) Surface area, Σ, vs the wall distance, X_b, over one pseudo-period of the zigzag for $Bo = 0.5$ and various Ga; (b) bubble cross section in the diametrical plane (Y'', Z'') perpendicular to the transverse motion at X_b positions midway between the centreline of the zigzag and its extremity closest to the wall (these positions are marked with circular symbols in panel a); the Y'' axis is parallel to the bubble minor axis and the Z'' axis is horizontal and parallel to the wall. (c,d) Same as (a,b) for $Ga = 70$ and various Bo. In all panels, the black and blue evolutions belong to the WMA regime. Solid (respectively, dashed) lines refer to the approaching (respectively, departing) stage. Values shown in (b,d) correspond to the frontal area, $S_\perp$, enclosed in the contour of the same colour, with the first and second numbers in each pair referring to the approaching and departing stages, respectively.

they perform oscillatory rigid-body rotations with an angular velocity that vanishes at the inflection points of the zigzags and reaches its maxima at their extremities. The more oblate the bubble is, hence the larger Bo, the larger its resistance to such rotational motions is. This is due on the one hand to the rapid increase of the viscous torque with χ (for a given rotation rate), and on the other hand to that of the moment of inertia of the liquid entrained by the rotational motion (so-called rotational added-mass coefficient), which governs the rate of change of the angular velocity. For instance, both quantities almost double from $\chi = 2$ to $\chi = 2.5$ when $Re \gg 1$ (Magnaudet 2011). This sharp increase limits severely the amplitude of the oscillatory rotations a bubble with a given volume may perform, which translates directly into a reduction in the amplitude of the zigzags. For instance, with $Ga = 70$, present simulations indicate that this amplitude decreases by a factor of two from $Bo = 0.25$ to $Bo = 1.5$ in the unbounded configuration, and a similar decrease may be observed in figure 15(c) in the presence of the wall. The above arguments concur to the conclusion that the NWZ regime can only exist within a finite range of χ, hence of Bo.

6. Summary

We carried out three-dimensional numerical simulations of the buoyancy-driven motion of freely deformable bubbles rising near a vertical wall in the parameter range $0.02 \leqslant Bo \leqslant 2$, $35 \leqslant Ga \leqslant 90$. Within this range, provided the Bond number exceeds a Ga-dependent threshold, $Bo_c(Ga)$, an isolated bubble immersed in an unbounded fluid follows a zigzagging or spiralling path, whereas it rises in a straight line if $Bo < Bo_c(Ga)$. In the latter case, the three distinct regimes of near-wall rising motions discussed at smaller Ga in Part 1, namely periodic near-wall bouncing, damped bouncing and migration away from the wall, are observed up to $Ga \approx 50$.

For larger Ga and small Bond numbers (typically $Bo < 0.05$ at $Ga = 60$ and $Bo \lesssim 0.1$ for $Ga \geqslant 70$), a new regime is found. In that BTE scenario, the bubble manages to escape from the wall region after one to two near-wall bounces. The escape mechanism is rooted in the abrupt flow reversal that takes place in the gap just before the bubble collides with the wall. This reversal is a consequence of the drop in the bubble rise speed which brings part of the fluid previously contained in the wake into the gap region. As a result, a strong rotational flow forms around the bubble surface, leading to a repulsive Magnus-like lift force that keeps a magnitude of the same order as the buoyancy force over a significant period of time after the collision. Bubbles are found to eventually escape from the wall region every time the spinning rate characterising the rotational flow at the bubble surface exceeds a critical value. A crude force balance allows the coefficient involved in the expression of the Magnus-like force to be estimated at around 0.5. In an unbounded domain, path instability takes place when $Bo \geqslant Bo_c(Ga)$. Paths of bubbles rising near a vertical wall are also found to experience transverse oscillations as soon as $Bo > Bo_c(Ga)$. This suggests that the wall plays little role in the occurrence of path instability. Its most significant effect appears to be the selection of the plane where the zigzagging motion takes place, which is always perpendicular to the wall. Simulations reveal that zigzagging or spiralling bubbles rising near a wall experience one of the following two scenarios.

For $Bo > Bo_c(Ga)$ and Ga up to 50, or $Bo > 1$ and larger Ga, bubbles ultimately migrate away from the wall, following a zigzagging motion for $Bo \lesssim 1.5$ and a spiralling motion at larger Bo, on which a small lateral drift superimposes. The same phenomenology is observed whatever Ga just above the critical curve, i.e. for $Bo \gtrsim Bo_c(Ga)$. In this WMA regime, the characteristics of the transverse path oscillations are very close to those determined in an unbounded domain. This is especially true regarding frequencies, be they those of the path oscillations themselves or those of the shape oscillations that develop under sufficiently supercritical conditions. In this regime, bubble wakes only interact weakly with the wall as soon as the gap thickness exceeds half of the bubble radius. Therefore, the repulsive interaction mechanism is essentially similar to that observed below the path instability threshold at lower Ga. The net migration away from the wall does not vary monotonically with the control parameters Ga and Bo. This is mostly due to the initial stages of the rise, during which the amount of time a given bubble spends close to the wall depends dramatically on the growth rate and saturated amplitude of the zigzags. For this reason, bubbles following paths with a slowly growing zigzagging component or performing lateral excursions with a moderate amplitude migrate faster.

For $Ga \geqslant 60$ and intermediate Bond numbers slightly larger than $Bo_c(Ga)$ but smaller than an upper value between 1 and 1.5, bubbles maintain a NWZ motion without migrating towards the bulk. The trapping phenomenon characterising this regime is a consequence of the intense interaction of the double-threaded wake with the wall during the stages when the gap comes to its minimum. The energy dissipation resulting from this wake–wall interaction translates into a severe drop in the rise speed, which in turn results in

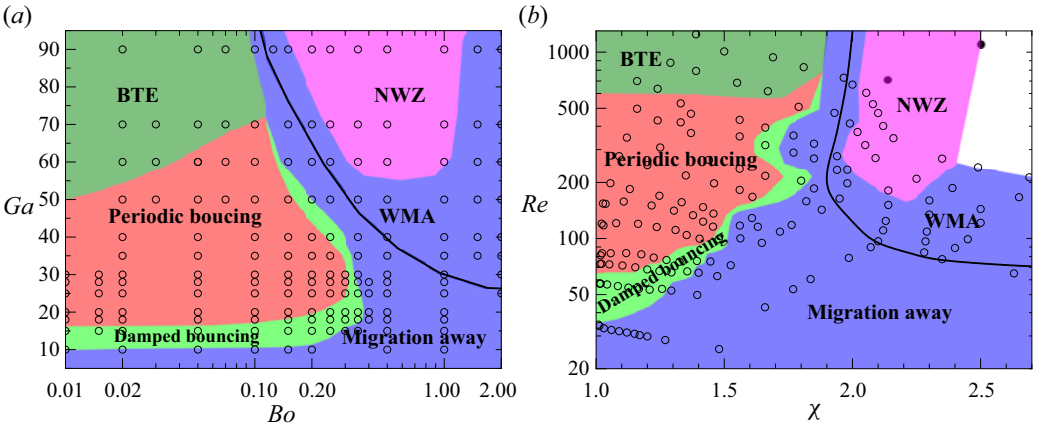

Figure 16. Complete state diagram of near-wall rising regimes observed in the simulations up to $Ga = 90$ and $Bo = 2$. Panels show (*a*) the (Bo, Ga)-plane; (*b*) the (χ, Re)-plane, with χ and Re determined as explained in the caption of figure 3. Solid line: neutral curve corresponding to the onset of path instability in an unbounded fluid (Bonnefis *et al.* 2024). The blue zone straddling the neutral curve represents the whole set of conditions under which bubbles migrate away from the wall, either in the presence or in the absence of path instability. In (*b*), the two bullets at (χ, Re) = (2.1, 710) and (χ, Re) = (2.5, 1100) correspond to experimental data from de Vries (2001) and Jeong & Park (2015), respectively. Both were obtained in water and show the persistence of the NWZ regime beyond the maximum Ga reached in the simulations.

a drastic transient reduction of the bubble oblateness. Because of this, the frontal area opposing the transverse motion is larger when the bubble departs from the wall than when it returns to it. This makes it possible for resistive transverse forces, such as viscous drag and added mass, to counteract the repulsive interaction force, maintaining the centreline of the zigzagging motion a constant distance from the wall. The mechanism at play requires the zigzag amplitude to be large enough for bubbles to be trapped. This is why this regime only exists up to a maximum Bond number, the lateral excursions of highly oblate bubbles being severely limited by viscous and inertial effects resisting the periodic rotation needed to keep such bubbles broadside on along their path.

Figure 16 gathers present results and those obtained at lower Ga in Part 1. It provides an overview of all the near-wall rising regimes we could identify for Ga up to 90 and Bo up to 2. This map allows a global assessment of the influence of fluid inertia and bubble deformation on the transitions between the various styles of path. For weakly deformed bubbles, say $Bo \lesssim 0.1$, the response of the system is largely controlled by the two antagonistic forces that both originate in fluid inertia, namely the repulsive force induced by the vortical wake–wall interaction mechanism summarised in § 1 and the attractive force resulting from the acceleration of the fluid in the gap, as predicted when the flow is assumed irrotational. The vortical effect dominates up to $Ga \approx 10$, making bubbles migrate away from the wall whatever Bo. The influence of the attractive irrotational effect increases gradually with increasing Ga (hence Re), driving bubbles towards the wall when $Ga \gtrsim 10$ (corresponding to $Re \gtrsim 35$). This attractive process gives rise to a damped near-wall bouncing regime up to $Ga \approx 17$, i.e. $Re \approx 65$, then to a periodic near-wall bouncing regime at higher Ga. The latter persists up to $Ga \approx 50$ at $Bo = 0.01$ and $Ga \approx 70$ at $Bo = 0.1$, which in both limits corresponds to $Re \approx 500$. For larger Ga, low-Bo bubbles escape from the wall region following the BTE scenario. In this regime, the mechanism responsible for the bubble escape may be viewed as a side effect of the above irrotational mechanism. Indeed, the intensity of the tumbling flow that forms around

the bubble surface during the collision with the wall depends crucially on the wall-ward velocity of the bubble and, thus, on the attractive force acting on it.

As Bo increases beyond 0.1, bubbles become more oblate in inertia-dominated regimes. The above two antagonistic effects are still at work, but their magnitude is strongly influenced by the bubble shape. In particular, deformation significantly enhances the repulsive vortical effect, owing to the increase of the tangential vorticity at the bubble surface with the local curvature of this surface. This promotes the migration away from the wall, as the (χ, Re) representation in figure 16(b) highlights. Below the path instability threshold, all bubbles with $Ga \leqslant 30$ (respectively, $Ga > 30$) migrate away from the wall as long as their aspect ratio exceeds ≈ 1.5 (respectively ≈ 1.8). In the presence of path instability, i.e. for $\chi \gtrsim 1.95$, bubbles still exhibit an average migration away from the wall, provided that the transient reduction in χ they experience when they get very close to the wall remains weak enough. This reduction becomes significant (say $\geqslant 5\,\%$) when $Ga \geqslant 60$ for intermediate Bond numbers such that $Bo_c(Ga) \lesssim Bo \lesssim 1$. In this high-$Ga$ intermediate-Bo range, bubbles are trapped near the wall, undergoing a zigzagging-like motion without being able to escape to the bulk.

The two parts of this study provide comprehensive insights into the complex dynamics of buoyancy-driven isolated bubbles rising near a vertical hydrophilic wall. This second part highlights the complex interplay between wake–wall interactions, wall-induced fluid displacements, time-dependent bubble deformation and, in the relevant parameter range, lateral bubble excursions resulting from path instability.

The findings obtained in this study form a solid basis for developing low-order predictive semi-empirical models of near-wall bubble motion under a broad range of flow conditions. However, to get closer to practical applications, one has to consider configurations more representative of wall-bounded bubbly suspensions. In this context, one key aspect is the influence of inhomogeneity in the ambient flow 'seen' by a test bubble. Inhomogeneity may arise due to the presence of a neighbouring bubble or because the carrying flow is non-uniform. In the first case, Huang *et al.* (2025) recently carried out simulations in which two identical bubbles initially arranged in line rise close to a vertical wall under moderately inertial conditions. They found that, due to the interaction with the leading bubble, the trailing bubble may escape from the wall, whereas the same bubble would bounce periodically close to the wall if it were rising alone. This change in the nature of the bubble dynamics highlights the need to consider interactions with neighbouring bubbles, especially if one is to predict the microstructure of the near-wall region in a bubbly suspension. A relevant and affordable follow-up to the above work would be its extension to the highly inertial regimes investigated in the present paper. Inhomogeneity also frequently arises through the non-uniformity of the carrying flow, especially when this flow is driven by a pressure gradient acting along the wall, such as in upward or downward pipe flows. In the upward configuration, it is well known that the shear-induced lift force tends to make nearly spherical or moderately deformed bubbles accumulate close to the wall, which is expected to strengthen wall–bubble interactions. Up to now, this problem has essentially been considered in weakly to moderately inertial regimes and quasi-steady conditions (Magnaudet, Takagi & Legendre 2003; Takemura, Magnaudet & Dimitrakopoulos 2009; Shi *et al.* 2020). Only recently has the exploration of wall-bounded shear flow configurations under highly inertial conditions, where bubbles undergo zigzagging motions, started (Su *et al.* 2024), with a focus on the time-averaged lateral force. How the non-uniformity in the ambient flow affects the nature of wall–bubble interactions, hence the bubble paths and eventually the time spent near the wall by bubbles experiencing such highly inertial conditions, is currently an open question. A numerical approach similar to that employed in the present study is appropriate to address it.

Another important issue to be considered in future research concerns surfactant-induced Marangoni effects. Indeed, in most systems, bubbles are contaminated by surfactants present in the fluid, especially with water. The associated surface tension gradients are expected to strengthen wake effects, hence repulsive forces. Moreover, interactions with the wall tend to make the surfactant distribution asymmetric, which in turn induces an additional transverse force. How the combination of these effects affects the near-wall bubble dynamics over the various flow regimes has to be considered in future studies to improve engineering models for wall-bounded bubbly flows.

Funding. P.S. acknowledges the funding of the Deutsche Forschungsgemeinschaft (DFG, German Research Foundation) through grant number 501298479.

Declaration of interests. The authors report no conflict of interest.

Appendix A. Preliminary numerical tests

Extensive preliminary tests were carried out to assess the reliability of the numerical approach. According to the benchmark test for rising bubbles in Basilisk (Popinet 2017), the temporal and spatial accuracies of the predictions depend largely on five parameters: the Courant–Friedrichs–Lewy number N_{CFL}, the standard tolerance in the Poisson solver T_ε, the grid refinement criteria for the phase fraction ζ_f and velocity ζ_u and the minimum grid size $\overline{\Delta}_{min}$. For the specific problem under consideration, the tests conducted in Part 1 confirmed that setting $N_{CFL} = 0.5$, $T_\varepsilon = 10^{-4}$, $\zeta_f = 10^{-3}$, $\zeta_u = 10^{-2}$ and $\overline{\Delta}_{min} = 1/68$ (further decreased to 1/136 when $\overline{\delta}_{min} \leqslant 0.15$) provides appropriately converged results. Specifically, the settings for the last two parameters guarantee a sufficient spatial resolution of the boundary layers at the wall and the bubble surface, as well as in the far wake ($\gtrsim 10R$ downstream from the bubble centroid) for Ga up to 30, the highest Ga considered in Part 1. In the present work, Ga goes up to 90, necessitating further verification of the values selected for these two parameters. For this purpose, we consider a case in the BTE regime with $(Bo, Ga) = (0.05, 90)$, for which the bubble Reynolds number (based on the terminal velocity and bubble diameter) is approximately 940. Therefore, with $\overline{\Delta}_{min} = 1/68$ (respectively $1/136$) and $\zeta_u = 10^{-2}$, approximately three (respectively six) cells lie in the boundary layer surrounding the bubble surface.

Figure 17 compares the predicted bubble motion for $(Bo, Ga) = (0.05, 90)$ using three different settings for $\overline{\Delta}_{min}$. For all three runs, ζ_u is fixed to 10^{-2}. Irrespective of $\overline{\Delta}_{min}$, the predicted lateral motion remains largely within the wall-normal plane, as the deviation of the bubble in the spanwise wall-parallel direction remains small, with Z_b never exceeding 0.2. The farthest wall-normal position where the bubble finally rests is approximately 6.75 with $\overline{\Delta}_{min} = 1/68$, while it is approximately 5.5, i.e. significantly closer to the wall, with $\overline{\Delta}_{min} = 1/136$. Close inspection of the predictions reveals that, as $\overline{\Delta}_{min}$ decreases from $1/68$ to $1/136$, the bubble reaches a slightly larger separation during the final reversal stage (inset in panel a), resulting in a lower peak in the departure velocity as it escapes from the near-wall region (consider the situation at $T \approx 12$ in panel c). The smaller final separation obtained with the finer grid follows. Conversely, the final rise speeds obtained with the different $\overline{\Delta}_{min}$ show no discernible difference (panel d). These observations prove the importance of a sufficient spatial resolution within the wall boundary layer, especially during stages of intense bubble–wall interaction, to accurately predict the final wall-normal position of the bubble. This is further corroborated by the good agreement observed between predictions with $\overline{\Delta}_{min} = 1/136$ and those adopting an adaptive $\overline{\Delta}_{min}$, where $\overline{\Delta}_{min} = 1/68$ is decreased to $1/136$ only during stages when $\overline{\delta}_{min}(T) \leqslant 0.15$.

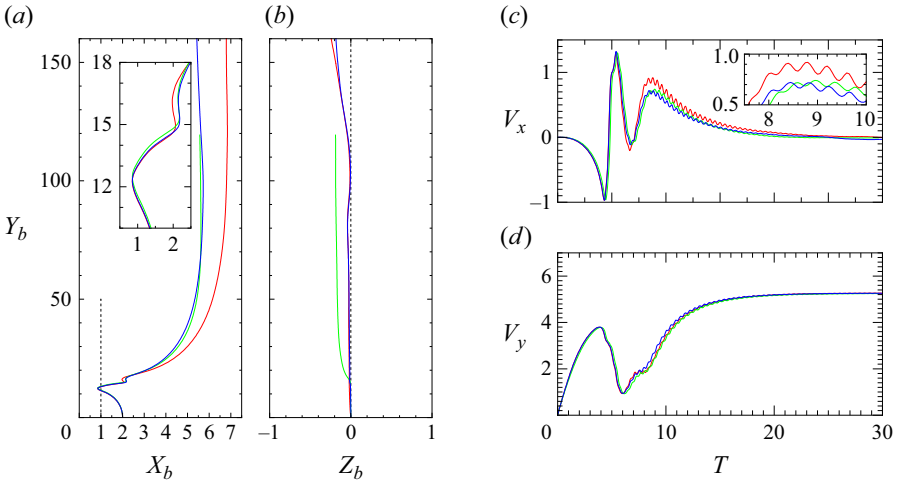

Figure 17. Effects of the minimum grid size on the predicted bubble motion for $(Bo, Ga) = (0.05, 90)$. Red and green lines correspond to cases with $\overline{\Delta}_{min} = 1/68$ and $1/136$, respectively, while the blue line refers to the case where $\overline{\Delta}_{min}$ is decreased from $1/68$ to $1/136$ only when $\overline{\delta}_{min} \leqslant 0.15$. Panels (a) and (b) show the bubble path in the wall-normal and wall-parallel planes, respectively; panels (c) and (d) show the evolution of the wall-normal (V_x) and vertical (V_y) velocities of the bubble centroid, respectively.

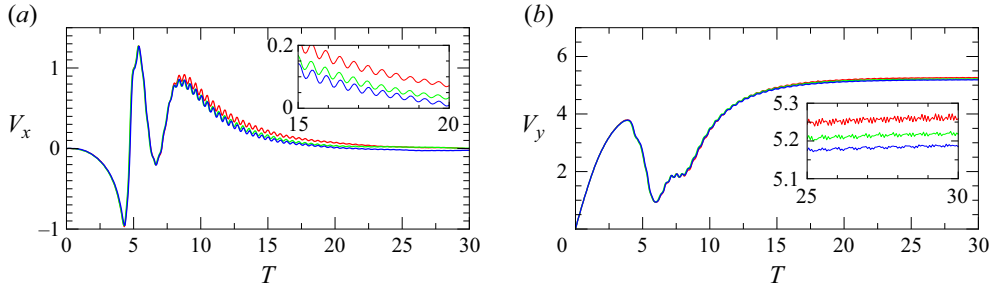

Figure 18. Effects of ζ_u on the predicted wall-normal (V_x) and vertical (V_y) velocities of the bubble centroid for $(Bo, Ga) = (0.05, 90)$. Red, green and blue lines correspond to predictions obtained with $\zeta_u = 10^{-2}$, 5×10^{-3} and 2×10^{-3}, respectively.

Effects of ζ_u are assessed based on the same test case. For this purpose, $\overline{\Delta}_{min}$ is set to $1/68$ and ζ_u is decreased from 10^{-2} to 2×10^{-3}, which decreases the cell size within the far wake from $1/17$ to $1/34$. With this refinement, the total number of grid cells when the boundary layer at the bubble surface is fully developed increases from 4.3 million to 21.8 million. Figure 18 compares the predictions obtained by varying ζ_u for the wall-normal and vertical bubble velocity components. It appears that the coarser resolution in the far wake leads to an underestimate of viscous effects. Specifically, the departing velocity (and to some minor extent the terminal rise speed) predicted with $\zeta_u = 10^{-2}$ is slightly larger than that obtained using smaller values of ζ_u. In contrast, predictions obtained with $\zeta_u = 5 \times 10^{-3}$ and $\zeta_u = 2 \times 10^{-3}$ exhibit only modest differences. Given this finding, and considering the significantly larger number of grid cells required with $\zeta_u = 2 \times 10^{-3}$ (21.8 million compared with 8.4 million), we set $\zeta_u = 5 \times 10^{-3}$ in all runs discussed in the paper.

Following the above observations and taking advantage of our prior preliminary tests in Part 1, we find it reasonable to set the five numerical parameters as follows: $N_{CFL} = 0.5$,

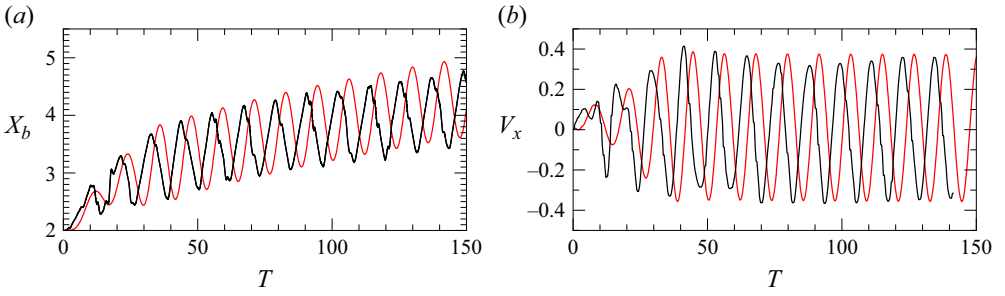

Figure 19. Comparison between predictions (red line, $(Bo, Ga) = (1, 35)$) and experimental results from Estepa-Cantero *et al.* (2024) (black line, $(Bo, Ga) = (0.97, 35)$) for the evolution of (*a*) the wall-normal position of the bubble centroid; and (*b*) the wall-normal velocity of the centroid.

$T_\varepsilon = 10^{-4}$, $\zeta_f = 10^{-3}$, $\zeta_u = 5 \times 10^{-3}$ and $\overline{\Delta}_{min} = 1/68$, automatically reduced to $\overline{\Delta}_{min} = 1/136$ when $\overline{\delta}_{min}(T) \leqslant 0.15$.

To further check the numerical approach, we carry out two additional runs belonging to different (Bo, Ga) ranges, for which reference data are available. First, we select $(Bo, Ga) = (1, 35)$, corresponding to an air bubble with $R \approx 1.46$ mm rising in silicone oil DMS-T05 ($Mo = 6.2 \times 10^{-7}$), as considered experimentally by Estepa-Cantero *et al.* (2024). Present predictions and experimental observations both conclude that the bubble departs from the wall and exhibits path oscillations in the wall-normal plane. Figure 19 shows how the results for the evolution of the wall-normal bubble position, X_b, and velocity, V_x, compare. Owing to differences in the bubble shape and rise speed in the initial state, differences are observed between the predicted and the experimental evolutions in the early stages of the near-wall motion. The agreement is fairly good in later stages, although slight deviations subsist in the maximum and minimum wall-normal position beyond $T \approx 100$. In the simulation, the Reynolds number based on the mean rise speed reached by the bubble when it moves far away from the wall ($X_b \geqslant 3$) is $Re \approx 110.6$, closely matching the value determined experimentally in the absence of the wall, $Re = 114.6$. Additionally, for $T \geqslant 100$, the crest-to-crest amplitude of the transverse oscillations, the magnitude of the maximum wall-normal velocity and the reduced frequency of the oscillations are $\overline{a} = 1.37$, $V_x^{max} = 0.370$ and $St = 0.108$ in the simulation, closely aligning with the experimental values $\overline{a} = 1.36$, $V_x^{max} = 0.358$ and $St = 0.104$.

In the second case, we consider a bubble rising from rest in an unbounded domain for $(Bo, Ga) = (0.134, 99)$. This parameter set corresponds to an air bubble with $R = 1$ mm rising in pure water at 20 °C ($Mo = 2.54 \times 10^{-11}$), a configuration already considered in experiments (Duineveld 1995; Tagawa *et al.* 2014). Figure 20 illustrates the evolution of the bubble path, velocity and aspect ratio, all obtained from the present simulation. The bubble successively follows a straight path, then a flattened helical path and finally tends to transition to a planar zigzagging path. This transition sequence differs from that reported by Tagawa *et al.* (2014), presumably due to the different initial conditions in the simulation and the experiment (Tchoufag, Fabre & Magnaudet 2015). Aside from this difference, the mean values for the rise speed V_y, the reduced frequency associated with the wall-normal velocity V_x (which is half that associated with V_y), and the bubble aspect ratio (averaged over the last five periods of oscillation of V_y) are $V_y = 3.55$, $St = 0.04$, $\chi = 2.14$, all in good agreement with the values from previous investigations, namely $V_y = 3.59$, $St = 0.038$, $\chi = 2.14$.

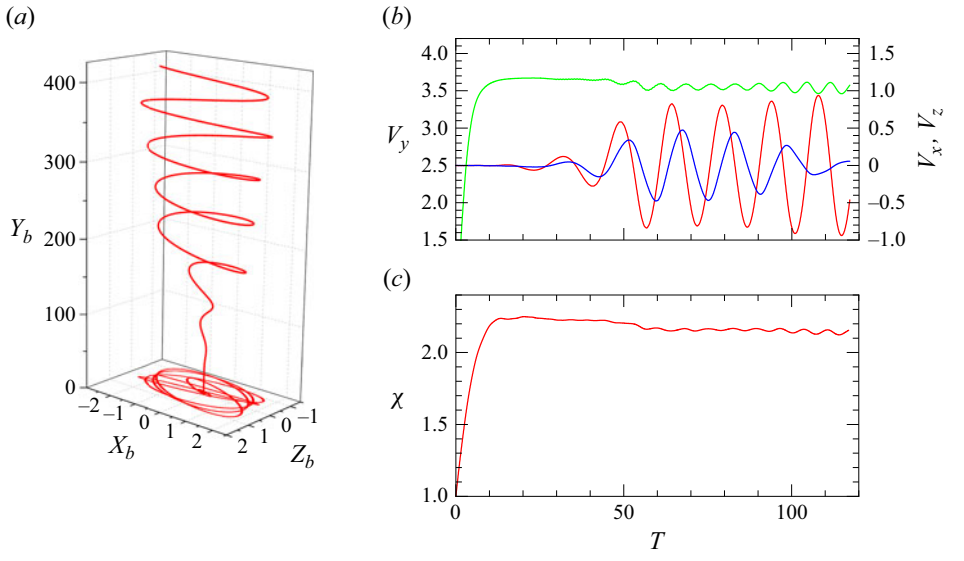

Figure 20. Predictions of the path characteristics of a single bubble with $(Bo, Ga) = (0.134, 99)$ rising from rest in an unbounded fluid domain. (*a*) Front and bottom views of the path; (*b*) evolution of the vertical (green line), and horizontal (red and blue lines) velocity components of the bubble centroid; (*c*) evolution of the bubble aspect ratio. The path eventually converges to a planar zigzagging motion in the (x, y) plane.

Appendix B. Influence of initial separation

The regime map gathering the various styles of path that are observed (figure 2*a*) was established based on simulations with an initial bubble–wall separation $X_0 = 2$. However, as the following discussion shows, this regime map remains unchanged when the initial separation is varied, provided that X_0 is not too large for wall effects to remain sizeable.

Below the neutral curve of path instability, four distinct scenarios take place. The influence of the initial separation on the first three of them (periodic near-wall bouncing, damped bouncing, migration away from the wall) was assessed in Part 1 (see Appendix C therein). In all cases it was found that X_0 only affects the initial stage of the bubble motion, leaving it unchanged in the fully developed state. Here, while Ga is larger, the mechanisms responsible for these three scenarios remain unchanged and so are the conclusions reached in Part 1. Figure 21 displays the influence of the initial separation in a case typical of the last of these four scenarios, the BTE regime. The corresponding (Bo, Ga) set is that considered in figure 6. All bubbles are found to eventually escape from the wall, since the final bubble–wall separation is large ($X_b(T \to \infty) > 6$) in all cases. The only noticeable effect of X_0 is that the bubble needs to bounce twice against the wall before escaping when it is released close enough to wall, typically for $X_0 \leqslant 2.0$. This is because the maximum wall-normal distance the bubble attains after a bounce depends largely on its impact velocity, which itself depends on the magnitude of the attractive force resulting from the irrotational Bernoulli mechanism. As figure 21(*b*) shows, the maximum rise speed achieved by the bubble before its first bounce decreases significantly with the initial separation when $X_0 \leqslant 2$, making the attractive force resulting from this mechanism (which goes like V_y^2) too weak to generate a large enough impact velocity during the first bounce in such cases.

For (Bo, Ga) sets located above the neutral curve, bubbles follow either a WMA or a NWZ scenario (figure 2*a*). In the former case, the wall dictates the orientation of the plane in which the bubble oscillates in the early stages. Nevertheless, once the saturated

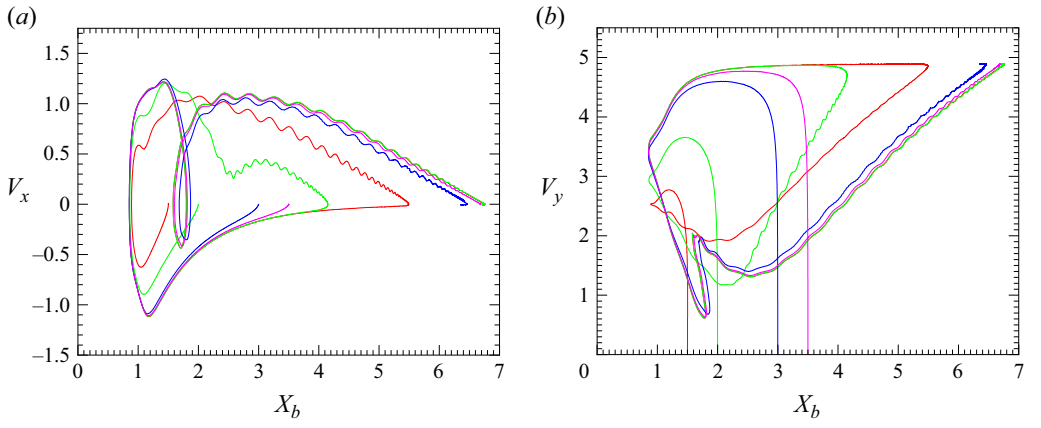

Figure 21. Influence of the initial separation, X_0, on the evolution of the two components of the centroid velocity in the BTE regime for a bubble with $(Bo, Ga) = (0.05, 70)$. (a) Wall-normal velocity, V_x; (b) vertical velocity, V_y. Red, green, blue and magenta lines correspond to initial separations $X_0 = 1.5$, 2.0, 3.0 and 3.5, respectively. The red and green curves overlap in the second half of the evolution.

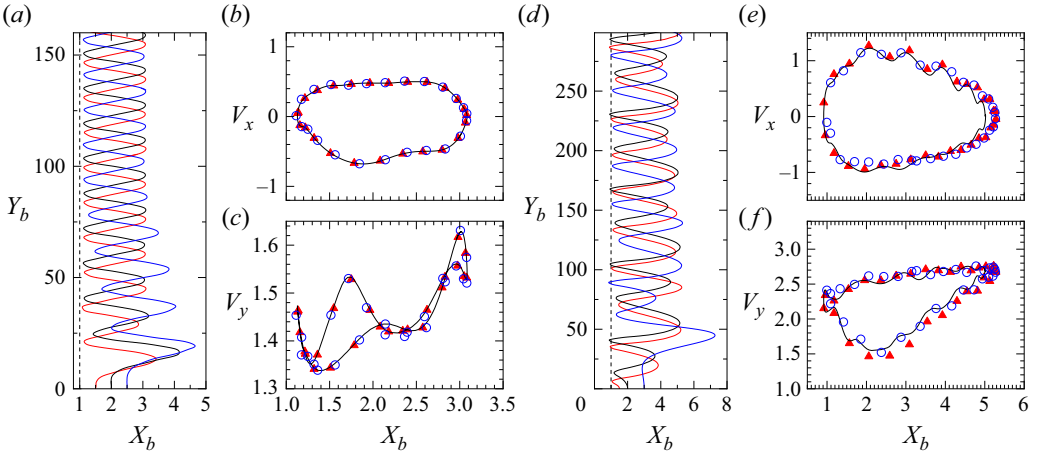

Figure 22. Paths and velocities of bubbles released at different initial separations. Panels $(a-c)$ and $(d-f)$ correspond to $(Bo, Ga) = (1, 70)$ and (0.25, 90), respectively. Black line: $X_0 = 2$; red line and triangles: $X_0 = 1.5$; blue line and circles: $X_0 = 2.5$ in $(a-c)$ and $X_0 = 3$ in $(d-f)$. The time interval between adjacent points in $(b-c, e-f)$ is 0.5. Evolutions in $(b-c)$ correspond to the last zigzagging period, while in $(e-f)$ they refer to the last cycle of path oscillations when the bubble collides with the wall.

state is reached, the characteristics of the motion are no longer affected by X_0. To reach this conclusion, we examined the two typical NWZ cases discussed in § 5.2, comparing results obtained with three different initial separations. Figure 22 shows the evolution of the bubble trajectory and velocity in these two cases. In the first of them (figure 22$a-c$), direct collisions with the wall do not take place. As the corresponding panels show, the path characteristics always converge towards a developed state where the vertical displacement and amplitude of the lateral drift during a single period no longer vary over the zigzagging period. Comparing the evolutions obtained with different X_0 confirms that the path characteristics in this fully developed state are independent of X_0. Accordingly, the evolutions of the wall-normal and vertical velocities of the bubble centroid collapse on

a single curve irrespective of X_0 (figure 22b–c). The initial separation only influences the time required to reach the developed state. Specifically, at the largest separation ($X_0 = 2.5$), five periods of transverse oscillations take place before the developed state is reached. This is way slower than in a periodic near-wall bouncing scenario where the developed state is reached after the second period of bouncing irrespective of X_0. This indicates a relatively long memory of the system with respect to the initial separation for bubbles evolving in the NWZ regime. This memory effect becomes more pronounced when Ga is large enough for bubble–wall collisions to take place (figure 22d–f). With $X_0 = 2$, the bubble path reaches a fully-developed state starting from the second bounce. In this developed stage, the amplitude of the lateral drift just after the collision is larger than that after the next or previous cycle of bouncing, where no collision takes place. In contrast, with $X_0 = 1.5$ and 3, a much larger number of zigzagging periods is required to reach a similar state (figure 22d). The evolution of the two components of the bubble velocity in the last zigzagging cycle where collision takes place is reported in panels (e–f). While the evolutions corresponding to the three different X_0 are close, there are still sizeable differences, which highlights the long memory of the system with respect to X_0 at large Ga and low-to-moderate Bo.

The non-negligible influence of X_0 has been reported in previous experiments with air bubbles rising near a wall in pure water (Jeong & Park 2015; Cai *et al.* 2023). These experiments were performed using bubbles with radii ranging from 1.14 to 1.96 mm, which corresponds to $120 \lesssim Ga \lesssim 270$. In most cases, these bubbles were found to follow the NWZ scenario reported here. Nevertheless, given the larger Ga, the memory effect related to the initial separation may last for much longer times than in present simulations, such that very long vertical displacements are required for the path to reach a fully developed state. It is even plausible that in these experiments, the vertical distance crossed by the bubble before it reaches the measurement window ($\approx 10R$ in Jeong & Park 2015 and $\approx 200R$ in Cai *et al.* 2023) is still not large enough for the corresponding memory effect to have completely faded away.

References

Auguste, F. & Magnaudet, J. 2018 Path oscillations and enhanced drag of light rising spheres. *J. Fluid Mech.* **841**, 228–266.

Bonnefis, P., Fabre, D. & Magnaudet, J. 2023 When, how, and why the path of an air bubble rising in pure water becomes unstable. *Proc. Natl Acad. Sci. USA* **120**, e2300897120.

Bonnefis, P., Sierra-Ausin, J., Fabre, D. & Magnaudet, J. 2024 Path instability of deformable bubbles rising in Newtonian liquids: a linear study. *J. Fluid Mech.* **980**, A19.

Cai, R., Ju, E., Chen, W. & Sun, J. 2023 Different modes of bubble migration near a vertical wall in pure water. *Korean J. Chem. Engng* **40**, 67–78.

Cano-Lozano, J.C., Martínez-Bazán, C., Magnaudet, J. & Tchoufag, J. 2016 Paths and wakes of deformable nearly spheroidal rising bubbles close to the transition to path instability. *Phys. Rev. Fluids* **1**, 053604.

Duineveld, P.C. 1994 Bouncing and coalescence of two bubbles in water. PhD thesis, University of Twente, The Netherlands.

Duineveld, P.C. 1995 The rise velocity and shape of bubbles in pure water at high Reynolds number. *J. Fluid Mech.* **292**, 325–332.

Ellingsen, K. & Risso, F. 2001 On the rise of an ellipsoidal bubble in water: oscillatory paths and liquid-induced velocity. *J. Fluid Mech.* **440**, 235–268.

Estepa-Cantero, C., Martínez-Bazán, C. & Bolaños Jiménez, R. 2024 Paths and wakes of deformable nearly spheroidal rising bubbles close to the transition to path instability. *Phys. Fluids* **36**, 013304.

Horowitz, M. & Williamson, C.H.K. 2010 The effect of Reynolds number on the dynamics and wakes of freely rising and falling spheres. *J. Fluid Mech.* **651**, 251–294.

HUANG, H., SHI, P., ELKINA, N., SCHULZ, H. & ZHANG, J. 2025 Path of a pair of deformable bubbles rising initially in line and close to a vertical wall. *Phys. Rev. Fluids* **10**, 023602.
JEONG, H. & PARK, H. 2015 Near-wall rising behaviour of a deformable bubble at high Reynolds number. *J. Fluid Mech.* **771**, 564–594.
JEONG, J. & HUSSAIN, F. 1995 On the identification of a vortex. *J. Fluid Mech.* **285**, 69–94.
KOK, J.B. 1993 Dynamics of a pair of gas bubbles moving through liquid Part I. Theory. *Eur. J. Mech. B Fluids* **12**, 515–540.
LAMB, H. 1932 *Hydrodynamics*. Cambridge University Press.
LEE, J. & PARK, H. 2017 Wake structures behind an oscillating bubble rising close to a vertical wall. *Intl J. Multiphase Flow* **91**, 225–242.
MAGNAUDET, J. 2011 A reciprocal theorem for the prediction of loads on a body moving in an inhomogeneous flow at arbitrary Reynolds number. *J. Fluid Mech.* **689**, 564–604.
MAGNAUDET, J. & MOUGIN, G. 2007 Wake instability of a fixed spheroidal bubble. *J. Fluid Mech.* **572**, 311–337.
MAGNAUDET, J., TAKAGI, S. & LEGENDRE, D. 2003 Drag, deformation and lateral migration of a buoyant drop moving near a wall. *J. Fluid Mech.* **476**, 115–157.
MEIRON, D.I. 1989 On the stability of gas bubbles rising in an inviscid fluid. *J. Fluid Mech.* **198**, 101–114.
MILOH, T. 1977 Hydrodynamics of deformable contiguous spherical shapes in an incompressible inviscid fluid. *J. Engng Maths* **11**, 349–372.
MOORE, D.W. 1963 The boundary layer on a spherical gas bubble. *J. Fluid Mech.* **16**, 161–176.
MOUGIN, G. & MAGNAUDET, J. 2002 Path instability of a rising bubble. *Phys. Rev. Lett.* **88**, 014502.
MOUGIN, G. & MAGNAUDET, J. 2006 Wake-induced forces and torques on a zigzagging/spiralling bubble. *J. Fluid Mech.* **567**, 185–194.
MUNDHRA, R., LAKKARAJU, R., DAS, P.K., PAKHOMOV, M.A. & LOBANOV, P.D. 2023 Effect of wall proximity and surface tension on a single bubble rising near a vertical wall. *Water* **15**, 1567.
POPINET, S. 2009 An accurate adaptive solver for surface-tension-driven interfacial flows. *J. Comput. Phys.* **228**, 5838–5866.
POPINET, S. 2015 A quadtree-adaptive multigrid solver for the Serre–Green–Naghdi equations. *J. Comput. Phys.* **302**, 336–358.
POPINET, S. 2017 Bubble rising in a large tank, Available at: http://basilisk.fr/src/examples/bubble.c.
RASTELLO, M., MARIÉ, J.L., GROSJEAN, N. & LANCE, M. 2009 Drag and lift forces on interface-contaminated bubbles spinning in a rotating flow. *J. Fluid Mech.* **624**, 159–178.
SHI, P. 2024 Reversal of the transverse force on a spherical bubble rising close to a vertical wall at moderate-to-high Reynolds numbers. *Phys. Rev. Fluids* **9**, 023601.
SHI, P., RZEHAK, R., LUCAS, D. & MAGNAUDET, J. 2020 Hydrodynamic forces on a clean spherical bubble translating in a wall-bounded linear shear flow. *Phys. Rev. Fluids* **5**, 073601.
SHI, P., ZHANG, J. & MAGNAUDET, J. 2024 Lateral migration and bouncing of a deformable bubble rising near a vertical wall. Part 1. Moderately inertial regimes. *J. Fluid Mech.* **998**, A8.
SU, Z., SUN, J., ZHANG, J., CAI, R., SUN, K., CHEN, W. & YU, C. 2024 Experimental investigation on dynamic characteristics of single bubble near wall in shear flow. *Phys. Fluids* **36**, 033323.
SUGIOKA, K.I. & TSUKADA, T. 2015 Direct numerical simulations of drag and lift forces acting on a spherical bubble near a plane wall. *Intl J. Multiphase Flow* **71**, 32–37.
TAGAWA, Y., TAKAGI, S. & MATSUMOTO, Y. 2014 Surfactant effect on path instability of a rising bubble. *J. Fluid Mech.* **738**, 124–142.
TAKEMURA, F. & MAGNAUDET, J. 2003 The transverse force on clean and contaminated bubbles rising near a vertical wall at moderate Reynolds number. *J. Fluid Mech.* **495**, 235–253.
TAKEMURA, F., MAGNAUDET, J. & DIMITRAKOPOULOS, P. 2009 Migration and deformation of bubbles rising in a wall-bounded shear flow at finite Reynolds number. *J. Fluid Mech.* **634**, 463–486.
TAKEMURA, F., TAKAGI, S., MAGNAUDET, J. & MATSUMOTO, Y. 2002 Drag and lift forces on a bubble rising near a vertical wall in a viscous liquid. *J. Fluid Mech.* **461**, 277–300.
TCHOUFAG, J., FABRE, D. & MAGNAUDET, J. 2015 Weakly nonlinear model with exact coefficients for the fluttering and spiraling motion of buoyancy-driven bodies. *Phys. Rev. Lett.* **115**, 114501.
VELDHUIS, C. 2007 Leonardo's paradox: path and shape instabilities of particles and bubbles. PhD thesis, University of Twente, The Netherlands.
VELDHUIS, C., BIESHEUVEL, A. & VAN WIJNGAARDEN, L. 2008 Shape oscillations on bubbles rising in clean and in tap water. *Phys. Fluids* **20**, 040705.
DE VRIES, A.W.G. 2001 Path and wake of a rising bubble. PhD thesis, University of Twente, The Netherlands.
DE VRIES, A.W.G., BIESHEUVEL, A. & VAN WIJNGAARDEN, L. 2002 Notes on the path and wake of a gas bubble rising in pure water. *Intl J. Multiphase Flow* **28**, 1823–1835.

VAN WIJNGAARDEN, L. 1976 Hydrodynamic interaction between gas bubbles in liquid. *J. Fluid Mech.* **77**, 27–44.

YAN, H., ZHANG, H., LIAO, Y., ZHANG, H., ZHOU, P. & LIU, L. 2022 A single bubble rising in the vicinity of a vertical wall: a numerical study based on volume of fluid method. *Ocean Engng* **263**, 112379.

ZENIT, R. & MAGNAUDET, J. 2008 Path instability of rising spheroidal air bubbles: a shape-controlled process. *Phys. Fluids* **20**, 061702.

ZENIT, R. & MAGNAUDET, J. 2009 Measurements of the streamwise vorticity in the wake of an oscillating bubble. *Intl J. Multiphase Flow* **35**, 195–203.

ZHANG, J., NI, M. & MAGNAUDET, J. 2021 Three-dimensional dynamics of a pair of deformable bubbles rising initially in line. Part 1. Moderately inertial regimes. *J. Fluid Mech.* **920**, A16.

ZHANG, Y., DABIRI, S., CHEN, K. & YOU, Y. 2020 An initially spherical bubble rising near a vertical wall. *Intl J. Heat Fluid Flow* **85**, 108649.